

# Determination of Time-Spatial Varying Mold Heat Flux During Continuous Casting from Fast Response Thermocouples



HAIHUI ZHANG and PENGCHENG XIAO

To ensure accurate estimation of mold heat flux, this study investigated the impacts of the thermocouples placement inserted in the mold wall, the temperature sampling rate ( $f_s$ ), and the noise level of temperature data on the precision of two-dimensional Inverse Heat Conduction Problem (2DIHCP). The results showed the accuracy of heat flux estimations decreases as the distance between the thermocouple and the mold surface increases, and it is recommended that the distance should not exceed 3 mm. The accuracy of the heat flux initially increases as  $f_s$  increases from 5 to 10 Hz, reaches a relatively stable state as  $f_s$  increases from 10 to 60 Hz, and eventually decreases as  $f_s$  increases from 60 to 100 Hz. Additionally, higher temperature measurement errors typically lead to decreased accuracy in inverse analysis. 2DIHCP was employed to compute the heat flux for a mold simulator experiment, and the results demonstrated its effectiveness in reconstructing the mold heat flux at the meniscus level during the time lapse of a mold oscillation cycle.

<https://doi.org/10.1007/s11663-023-02925-y>

© The Minerals, Metals & Materials Society and ASM International 2023

## I. INTRODUCTION

THE continuous casting of molten steel is a vital process in modern steelmaking, where molten steel is poured into a water-cooled mold and continuously extracted as a solidified strand. During the initial stages of molten steel solidification, heat is transferred from the steel to the mold, affecting the surface quality of the solidified strand.<sup>[1]</sup> Accurate measurement of mold heat flux is essential for understanding the heat transfer mechanism, optimizing the casting process, and preventing defects in the solidified strand.<sup>[2–6]</sup>

The measurements of mold heat flux are performed by determination of the temperature gradients in the copper plate of the mold using thermocouples inserted in the mold wall, and/or by determination of the increase of the temperature of the cooling water.<sup>[7]</sup> The mold heat flux,

especially in the vicinity of the mold meniscus area, where the initial shell thickness is within 5 mm, plays a critical role in determining the surface quality of the steel strands.<sup>[8]</sup> The mold heat flux can display oscillations over time. When transient measurements of heat flux are taken at the meniscus level, oscillating fluctuations in heat flux can be observed. These oscillations are not propagated to the rest of mold.<sup>[9]</sup> The further studies<sup>[10–12]</sup> have shown that the mold heat transfer signal consists of low- and high-frequency components. The heat flux with a frequency less than half of the mold oscillation frequency is categorized as a low-frequency mold heat flux. This type of heat flux is associated with low-frequency phenomena, such as solidification shrink, unevenness growth of the shell, melt flows, and level fluctuations. On the other hand, the heat flux near the liquid slag surface has a high-frequency signal with a frequency equal to the mold oscillation frequency. This high-frequency heat flux corresponds to high-frequency phenomena, such as oscillation mark formation, partial meniscus solidification, and so on. Along the casting direction, the high-frequency heat flux signal tends to weaken. Thus, transient measurements of mold heat flux can provide insight into the different mechanisms at work in the mold.

The temperature data may not capture the full range of temperature variations within the mold if the temperature sampling rate is too low. This is because high-frequency temperature variations are incorrectly represented as lower frequency components in the data, resulting in inaccurate heat flux estimates. In order to measure the solidification phenomena occurring at

HAIHUI ZHANG is with the Faculty of Materials Metallurgy and Chemistry, Jiangxi University of Science and Technology, Ganzhou 341000, P.R. China and also with the Hebei High Quality Steel Continuous Casting Technology Innovation Center, Tangshan 063009, Hebei, P.R. China. PENGCHENG XIAO is with the College of Metallurgy and Energy, North China University of Science and Technology University, Tangshan 063210, P.R. China and also with the Hebei High Quality Steel Continuous Casting Technology Innovation Center. Contact e-mail: xiaopc@ncst.edu.cn

Manuscript submitted May 8, 2023; accepted September 15, 2023.

Article published online October 2, 2023.

different time scales and frequencies, Shannon sampling theorem<sup>[13]</sup> dictates that the sampling frequency  $f_s$  must be greater than the Nyquist frequency ( $2f_h$ ),  $f_s \geq 2f_h$ , where  $f_h$  is the highest frequency of the signal. Therefore, to monitor the change of heat flux during a mold oscillation cycle, the temperature sampling frequency must be high enough. Currently, the highest reported frequency exceeds 50 Hz<sup>[9,10]</sup> for thermocouples and 250 Hz<sup>[14]</sup> for optical fiber temperature sensors.

The conventional technique of determining temperature gradient with two thermocouples cannot be used to directly measure heat flux at the meniscus due to the transient temperature field of the mold, especially at the mold meniscus area where significant heat flow longitudinally upwards to the cold top of the mold. As a result, the methods of inverse heat conduction problems must be employed when the heat flux is estimated from the observed temperatures. But high-temperature sampling rate might increase computational complexity of the heat flux estimations by inverse methods. Additionally, a high sampling rate can introduce a large amount of noise in the temperature data due to sensor measurement errors, leading to a reduction in accuracy in heat flux estimation. Previous studies<sup>[15,16]</sup> have demonstrated that increasing the temperature sampling rate might decrease the accuracy of heat flux estimation by inverse problem. Therefore, it is crucial to investigate the effects of temperature sampling rate on the accuracy of mold heat flux estimation using inverse methods.

Temperature measurements are commonly used to monitor heat flux, which is important for improving cooling systems, casting practices, and process control. For example, too low a heat extraction rate will lead to breakouts, too high a rate to longitudinal cracks.<sup>[9,17,18]</sup> To measure heat flux distribution over the entire mold face, an array of thermocouples is typically embedded into the mold wall. Although this method is accurate and easy to use, it can be intrusive and may impact the mold's thermal behavior.<sup>[19]</sup> Alternatively, optical fibers have emerged as a promising technology for measuring mold heat flux, offering high accuracy, fast response, and immunity to electromagnetic interference.<sup>[20]</sup> The accuracy of heat flux estimations by inverse methods using the measured temperatures depends on various factors, including the location and measurement accuracy of the temperature sensor.<sup>[21,22]</sup> The accuracy can be improved if the sensor is placed near the boundary of the unknown heat flux.<sup>[15,21]</sup> Therefore, it is important to investigate the influences of the location and measurement accuracy of the temperature sensor on the accuracy of the heat flux estimations.

In the field of steel continuous casting, the first attempts to use inverse problem methods for determining the mold heat flux using the observed temperatures were made by Brimacombe.<sup>[23]</sup> Brimacombe *et al.* established an inverse problem of two-dimensional steady state heat transfer using the zeroth-order regularization method for estimating the mold heat flux. Thomas *et al.*<sup>[24]</sup> introduced an inverse heat conduction problem to estimate the heat transfer at the meniscus using the measured temperatures. The model can gain a better understanding of how heat is transferred at the mold meniscus area. Talukdar *et al.*<sup>[22]</sup>

employed a Salp Swarm Algorithm-based inverse heat transfer approach to predict mold heat flux. This method was utilized for parameter estimation within a three-dimensional steady-state thermal environment. Yao and Wang *et al.*<sup>[25,26]</sup> developed a two-dimensional transient inverse heat transfer problem by employing a nonlinear estimation technique. This approach facilitates enhanced comprehension of the nonuniform heat transfer dynamics within the continuous casting mold. Consequently, it enables the identification of previously unknown thermal resistances existing between the mold and the solidifying shell. Goldschmit *et al.*<sup>[27,28]</sup> developed an inverse analysis model employing the regularization method. This model facilitates the evaluation of mold heat flux based on the temperature data acquired from thermocouples embedded within the mold wall. Talukdar *et al.*<sup>[29]</sup> developed an inverse problem of steady state heat transfer by employing the conjugate gradient method to determine the mold heat flux from observed temperatures. Wang *et al.*<sup>[30]</sup> developed a two-dimensional transient inverse heat conduction problem using the whole-time domain conjugate gradient method to estimate the mold heat flux. Jayakrishna *et al.*<sup>[31]</sup> developed a three-dimensional steady-state inverse heat conduction problem to estimate mold heat flux through parameter estimation.

Inverse heat transfer problems are often classified as classical ill-posed problems, indicating that a solution may not exist, and even if it does, it could potentially be unstable or lack uniqueness. As a result, stabilization techniques are necessary to obtain reliable results for the inverse problem.<sup>[32]</sup> Stabilization techniques for inverse problems can be classified into gradient-based methods, such as the Levenberg–Marquardt method,<sup>[33–36]</sup> the function specification method,<sup>[37]</sup> the regularization method,<sup>[38]</sup> and the conjugate gradient method,<sup>[21,30,39]</sup> and stochastic-based methods, such as the Bayesian method,<sup>[40]</sup> the fuzzy inference method,<sup>[41]</sup> and the deep neural network algorithms.<sup>[42,43]</sup> Additionally, when dealing with transient heat transfer phenomena, the time domain over which measurements are utilized in the inverse problem can aid in categorizing the solution methods. Three distinct time domain methods have been proposed: (1) only to the present time, (2) to the present time plus a few time steps, and (3) the complete time domain. Methods based on the time domains (1) and (2) are sequential in nature. In the first method, the use of measurements only to the present time (1) is also called the Stolz method. In the second method, a few future temperatures (2) are used, originally proposed by Beck,<sup>[15]</sup> and the associated algorithms are called Beck's sequential method. However, sequential methods based on the time domains (1) and (2) generally become unstable as small-time steps are used in the analysis. The whole-time domain approach (3) is powerful because very small-time steps can be taken but it is not as computationally efficient. The majority of stabilization techniques, such as function specification, conjugate gradient method, and regularization methods, are applicable to both sequential and whole domain estimation forms.<sup>[15,39,44]</sup>

In order to effectively monitor the variation of mold heat flux during each mold oscillation cycle, the sequential method is deemed more suitable than the whole-time domain approach. This can be attributed to the time

delay present in the latter method during the feedback computation of the heat flux. In the engineering community, sequential function specification method developed by Beck has been widely used and successful in solving one-dimensional inverse heat conduction problems for more than 50 years.<sup>[45]</sup> In this method, the heat flux is assumed to be a constant or linear function over several number of future time steps, and then the stability of the solution in the time domain can be improved by selecting an appropriate number of future time steps.<sup>[15]</sup> As demonstrated by Beck,<sup>[15]</sup> the sequential method is preferred due to it is so much more efficient and gives only slightly different results from the whole domain method. Nevertheless, elevating the temperature sampling rate, which consequently reduces the time step within the sequential method, often results in a compromise in the precision of heat flux reconstruction. This is particularly pronounced in scenarios involving the heat flux that varies both spatially and temporally in the context of two- and three-dimensional heat transfer problems.<sup>[16,46,47]</sup> Furthermore, the function of heat flux might exhibit discontinuities. Effectively handling the discontinuity function form of the unknown remains a hot topic within the realm of inverse problem research. Tourn *et al.*<sup>[48]</sup> highlighted that the incorporation of such a regularization term enables the accurate capture of jump discontinuities present within the unknown function.

Therefore, a sequential regularization method based two-dimensional Inverse Heat Conduction Problem (2DIHCP) was proposed to estimate the mold flux using the temperatures measured by thermocouples.

Subsequently, an exploration was undertaken to analyze the impact of thermocouples parameters, such as the depth of thermocouples beneath mold surface ( $w_1$ ), the temperature sampling rate ( $f_s$ ), and the noise level of temperature data ( $\sigma$ ), on the precision of the 2DIHCP. Finally, 2DIHCP is applied to reconstruct heat flux across oscillating mold hot surface for a mold simulator runs.

## II. THE METHODOLOGY

### A. The Experimental

The trial of continuous casting was performed using a mold simulator, as illustrated in Figure 1. The mold simulator comprises an induction furnace, a water-cooled copper mold, a shell withdrawal mechanism (extractor), and a fast thermal monitoring system. The inverse-type water-cooled copper mold (30 mm × 50 mm × 350 mm) with oscillation capability was utilized in the mold simulator. The mold has a U-shaped water-cooling groove with 10 mm diameter internally, with a water inlet and outlet situated at the quarter-width and three-quarter-width positions of the mold, respectively. The mold was placed in an extractor so that only one face was exposed to the liquid melt. The mold and extractor, initially at room temperature, were then submerged into the molten steel and held for a few seconds, allowing a shell to solidify normal to the external surface. Subsequently, the extractor drew the solidifying shell downwards, enabling the fresh molten steel to come in contact with the mold for subsequent solidification, similar to the start-up of a continuous casting process.

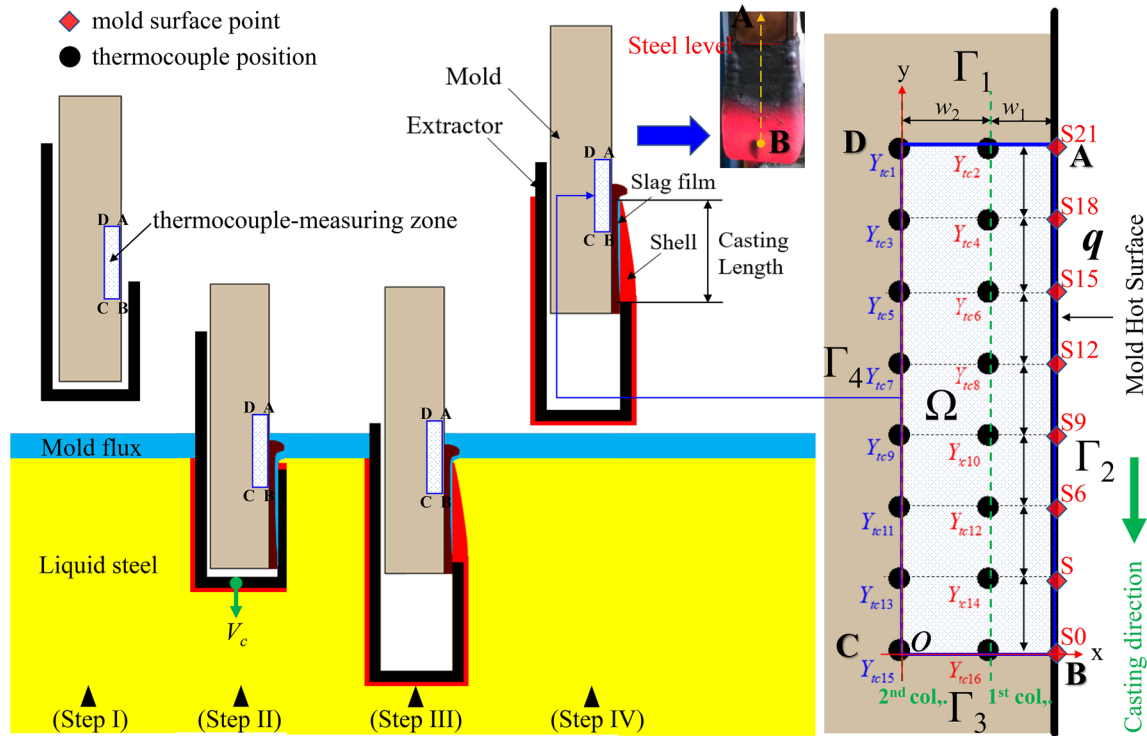


Fig. 1—Mold simulator apparatus and the locations of thermocouples inside the mold wall.

As shown in Figure 1, two columns of T-type thermocouples ( $2 \times 8$ ) are embedded at different depths along the centerline of the mold wall, positioned 3 and 8 mm away from the hot surface (AB) of the mold and separated by 3 mm vertically. Sixteen highly sensitive T-type thermocouples, with a diameter of 0.5 mm, were used to measure the corresponding mold temperatures at a sampling frequency of 60 Hz, using a data acquisition system. The temperature of the second column of thermocouples located on the boundary  $\Gamma_4$  (CD) was used to determine the temperature boundary condition  $f^*(t^*)$ . This was achieved by interpolating the linear correlation between the two adjacent measured temperatures for the nodes situated between the two thermocouples. This configuration of thermocouples in the mold was chosen selected based on the research of Badri *et al.*<sup>[49]</sup> Furthermore, the temperature history of the first column of thermocouples, denoted as a vector  $\mathbf{T} \in \mathbb{R}^M$ , will be utilized to develop the inverse problem for determining the mold surface heat flux.

The experiment proceeded in the following manner: 30 kg of medium carbon steel was melted in an induction furnace with a MgO lining and an argon atmosphere of 99.99 pct purity. The temperature of the molten steel was then adjusted to the target value to control the superheat. Metal Al (~100 g) was added to the molten steel as a deoxidizer. Subsequently, a layer of decarburized molten flux (0.5 kg) was added to the surface of the molten steel to create a layer of molten flux 6 to 9 mm thick on the top of the liquid steel. Step I: After submerging the oscillating water-cooled copper mold and extractor into the melt at the target depth, the level of molten steel was located in the thermocouple-measuring zone of the mold. Step II: the mold and extractor were held for several seconds to form an initial shell normal to the external surface of the mold, ensuring that the initial shell was strong enough to prevent tearing during extraction. Step III: The extractor then withdrew the solidifying shell downward at a constant speed to simulate continuous casting, while the mold moved upward at a certain speed to compensate for the rise in the mold level, so that the level of liquid melt remained in the same position relative to the mold. Step IV: Upon completion of the casting, the mold and extractor along with the attached steel shell were removed from the melt and cooled to room temperature. Throughout this process, the mold was kept oscillating sinusoidally at the pre-set frequency and stroke from the time it was submerged into the molten steel until the casting was completed.

Due to the presence of an air gap between the mold and the extractor, the heat transfer from the mold to the extractor can be considered negligible. Therefore, the heat transfer along the central line of the mold in the casting direction is considered two-dimensional (2D). As a result, the heat transfer within the rectangular area ABCD of the mold, represented in Figure 1 and denoted as  $\Omega^*$ , is considered two-dimensional. The rectangular area, ABCD, with a height (AB)  $H^*$  of 21 mm and a width (BC)  $W^*$  of 8 mm consists of four boundary conditions represented by  $\Gamma_1$  (DA),  $\Gamma_2$  (AB),  $\Gamma_3$  (BC), and  $\Gamma_4$  (CD). Since the temperature of the mold wall is between 300 K and 600 K,<sup>[10,50]</sup> it is reasonable to assume that the material properties of the mold (heat

capacity, density, and thermal conductivity) remain constant. The direct problem of investigating 2D heat transfer in the ABCD rectangular area is governed by the Fourier heat transfer partial differential equation with corresponding thermal boundary conditions.

$$\rho c \frac{\partial T^*}{\partial t^*} = \lambda \Delta T^*, \text{ in domain } \Omega^* = [0, W^*] \times [0, H^*] \quad [1a]$$

$$-\lambda \frac{\partial T^*}{\partial \mathbf{n}} \Big|_{\Gamma_1 \cup \Gamma_2 \cup \Gamma_3} = \mathbf{q}^*, \text{ unknown} \quad [1b]$$

$$T^*(\Gamma_4, t^*) = f^*(t^*), \text{ measured} \quad [1c]$$

$$T^*(x^*, y^*, 0) = T_{\text{int}}^*, \quad [1d]$$

where  $\rho$  is the density in  $\text{kg m}^{-3}$ ,  $c$  represents the specific heat in  $\text{J kg}^{-1}$ ,  $T^*$  is the temperature in  $\text{K}$ ,  $t^*$  is the time in second,  $\lambda$  is the thermal conductivity in  $\text{W m}^{-1} \text{K}^{-1}$ ,  $\mathbf{q}^*$  is the heat flux to be estimated for the boundary conditions of  $\Gamma_1$ ,  $\Gamma_2$ , and  $\Gamma_3$  with the unit in  $\text{W m}^{-2}$ ,  $\mathbf{n}$  is the outer normal of boundary.  $f^*(t^*)$  is the temperature boundary condition on  $\Gamma_4$  with the unit in  $\text{K}$ .

## B. Definition of the Inverse Problem

The fundamental principle of inverse problems is to find the unknown heat flux  $\mathbf{q}$ , subsequently using this heat flux  $\mathbf{q}$  to calculate the temperature  $\mathbf{T}$  in a manner that results in a perfect fit between  $\mathbf{T}$  and the observed temperatures  $\mathbf{Y}$ . Therefore, the inverse heat conduction problem can be represented as an optimization problem with partial differential equation (PDE) constraints.<sup>[32]</sup> That is,

$$\min s = \sum_{i=1}^r \|\mathbf{Y}^{i+i-1} - \mathbf{T}^{i+i-1}\|^2 + \alpha \|\mathbf{h}_d \mathbf{q}^j\|^2. \quad [2a]$$

$$s.t. \quad \frac{\partial T}{\partial t} = \Delta T, \quad t_j \leq t \leq t_{j+r-1} \text{ in } \Omega = [0, W] \times [0, H] \quad [2b]$$

$$-\frac{\partial T}{\partial \mathbf{n}} \Big|_{\Gamma_1 \cup \Gamma_2 \cup \Gamma_3} = \mathbf{q}^j, \text{ to be estimated} \quad [2c]$$

$$T(\Gamma_4, t) = f(t), \text{ measured} \quad [2d]$$

$$T(x, y, t_j) = T_{\text{ini}}. \quad [2e]$$

All variables in Eqs. [2a] through [2e] are dimensionless. The dimensionless quantities were defined as follows:

$$T = \frac{T^* - T_{\text{ref}}}{\Delta T}, \quad Y = \frac{Y^* - T_{\text{ref}}}{\Delta T}, \quad \Delta T = \frac{q_{\text{ref}} L_{\text{ref}}}{\lambda}, \quad \mathbf{q}^j = \frac{\mathbf{q}^{j*}}{q_{\text{ref}}}, \quad (x, y) = \frac{(x^*, y^*)}{L_{\text{ref}}}, \quad t = \frac{\lambda t^*}{\rho c L_{\text{ref}}^2}.$$

Here,  $r$  ( $\geq 1$ ) is the number of future time steps. The Finite Difference Method (FDM)<sup>[51]</sup> is employed to solve the above direct problem of partial differential equation given by Eqs. [2b] through [2e]. In this approach, the computational domain ( $\Omega$ ), ABCD, is discretized into an  $n_x \times n_y$  uniform grids, with the boundaries  $\Gamma_1$ ,  $\Gamma_2$ , and  $\Gamma_3$  split into  $n_1$  ( $=n_x$ ),  $n_2$  ( $=n_y$ ), and  $n_3$  ( $=n_x$ ) divisions, respectively. Then, the unknown heat flux  $\mathbf{q}^j$  ( $= [\mathbf{q}_1^j, \mathbf{q}_2^j, \mathbf{q}_3^j]^T$ )  $\in \mathbb{R}^N$  at time  $t_j$  is denoted as a vector with  $N$  ( $= n_1 + n_2 + n_3$ ) components.  $\mathbf{q}_1^j$ ,  $\mathbf{q}_2^j$ , and  $\mathbf{q}_3^j$  are vectors of dimensions  $n_1 \times 1$ ,  $n_2 \times 1$ , and  $n_3 \times 1$ , corresponding to the heat fluxes on  $\Gamma_1$ ,  $\Gamma_2$ , and  $\Gamma_3$ , respectively.  $\|\cdot\|$  denotes the standard Euclidean norm. The right-hand side of Eq. [2a] contains a spatial regularization term,  $\alpha \|\mathbf{h}_d \mathbf{q}^j\|^2$ , which is used to penalize the spatial variation of the predicted heat flux.<sup>[15,48,52–55]</sup> There are three types of spatial regularizations: zeroth-, first-, and second-order.  $\alpha$  ( $>0$ ) is the regularization parameter,  $d$  is 0, 1 and 2 represent the order of spatial regularization.

$$\mathbf{q}^j = \underbrace{[q_1^j, q_2^j, \dots, q_{n_1}^j]}_{\mathbf{q}_1^j}, \underbrace{[q_{n_1+1}^j, q_{n_1+2}^j, \dots, q_{n_1+n_2}^j]}_{\mathbf{q}_2^j}, \underbrace{[q_{n_1+n_2+1}^j, q_{n_1+n_2+2}^j, \dots, q_N^j]}_{\mathbf{q}_3^j}^T. \quad [3]$$

$$\mathbf{Y}^j = [Y_1^j, Y_2^j, \dots, Y_M^j]^T \quad [4]$$

$$\mathbf{T}^j = [T_1^j, T_2^j, \dots, T_M^j]^T, \quad [5]$$

where both  $\mathbf{Y}^j$  and  $\mathbf{T}^j$  are  $M \times 1$  temperature vector at time  $t_j$ ,  $M$  is the number of measurements.  $q_n^j$  is the  $n$ -th component of heat flux  $\mathbf{q}^j$  at the time  $t_j$ .  $Y_m^j$  and  $T_m^j$  are the measured and the calculated temperature at the position  $m$  and the time of  $t_j$ , respectively.

$\mathbf{h}_d$  is  $d$ th-order spatial derivative operator acting on three different boundary heat fluxes (Table I).<sup>[15,48,52–55]</sup> In zeroth-order regularization ( $d = 0$ ),  $\alpha \|\mathbf{h}_d \mathbf{q}^j\|^2$  is the penalization for the magnitude of heat fluxes. In first-order regularization ( $d = 1$ ),  $\mathbf{h}_d \mathbf{q}^j$  can be interpreted as an approximation of the spatial gradient of the heat flux. In second-order regularization ( $d = 2$ ),  $\mathbf{h}_d \mathbf{q}^j$  can be interpreted as an approximation of the second-order spatial derivative of the heat flux. Moreover, first-order regularization constrains solutions with large spatial gradients, whereas second-order regularization penalizes solutions that have considerable second-order spatial derivatives. Furthermore, it is possible for heat flux,  $\mathbf{q}$ ,

to be discontinuous at the intersection points between two neighboring boundaries, such as the points **A** and **B** in Figure 1. Consequently, the spatial regularizations are individually applied for each boundary heat flux of  $\Gamma_1$ ,  $\Gamma_2$ , and  $\Gamma_3$ . Then,  $\mathbf{h}_d$  is defined as follows:

$$\mathbf{h}_d = \text{blkdiag}(\mathbf{h}_{d,1}, \mathbf{h}_{d,2}, \mathbf{h}_{d,3}). \quad [6]$$

The minimization of the objective function Eq. [2] can be achieved by taking the partial derivative of Eq. [2] with respect to the vector of  $\mathbf{q}^j$ , setting this equal to zero. This yields an estimator for unknown heat flux  $\mathbf{q}^j$ .

$$\mathbf{q}^j = \left( \sum_{i=1}^r \mathbf{J}_i^T \mathbf{J}_i + \alpha \mathbf{h}_d^T \mathbf{h}_d \right)^{-1} \left\{ \sum_{i=1}^r \mathbf{J}_i^T (\mathbf{Y}^{j+i-1} - \tilde{\mathbf{T}}^{j+i-1}) + \sum_{i=1}^r \mathbf{J}_i^T \mathbf{J}_i \mathbf{q}^* \right\}. \quad [7]$$

Here,  $\tilde{\mathbf{T}}^{j+i-1}$  is the temperature calculated by using the assumed heat flux  $\mathbf{q}^*$ . Usually,  $\mathbf{q}^*$  is an *a priori* estimate of  $\mathbf{q}^j$ .  $\mathbf{q}^* = \mathbf{q}^{j-1}$  is a common choice. However,  $\mathbf{q}^*$  can be set to zero if no *a priori* information about the heat flux is available, which will consequently reduce the computations required.<sup>[15]</sup>  $\mathbf{J}_j$  is called as the  $M \times N$  sensitivity coefficient matrix at time  $t_j$ , and could be obtained by solving the sensitivity coefficient problem given in Appendix A.

### C. Method of Solving the Inverse Problem

#### 1. Stopping criteria

If no measurement error in the temperature, the traditional stopping criteria for Eq. [2] is given by

$$s \leq \varepsilon_1 \quad [8]$$

$$\left\| \sum_{i=1}^r \mathbf{J}_i^T (\mathbf{Y}^{j+i-1} - \tilde{\mathbf{T}}^{j+i-1}) \right\| \leq \varepsilon_2, \quad [9]$$

where  $\varepsilon_1$  and  $\varepsilon_2$  are user-prescribed tolerances, and both values default to  $10^{-3}$ .

However, if the observed temperature data contain measurement error, Morosov's criterion states that the squared difference between the measured temperature  $\mathbf{Y}^\sigma$  and the calculated temperature  $\mathbf{T}$  should tend toward  $M\sigma^2$ , where  $M$  is the quantity of temperature measurements and  $\sigma$  is the constant standard deviation of the temperature measurement error.<sup>[56]</sup>

$$\|\mathbf{Y}^\sigma - \mathbf{T}\|^2 \approx M\sigma^2 \quad [10]$$

#### 2. Regularization parameter selection methods

Morosov's criterion suggests that the selection of the regularization parameter  $\alpha$  should be contingent upon the noise level of the observed temperature  $\sigma$ , such that the difference between the measured temperature  $\mathbf{Y}^\sigma$  and the calculated temperature  $\mathbf{T}$  is of the same magnitude as the measurement errors. A function is defined to facilitate this selection process.

**Table I. Three Different Derivative Operators for Spatial Regularization**

Regularization Method	Derivative Operator $\mathbf{h}_{d,i}$ , $i = 1, 2, 3$
Zeroth Order ( $d = 0$ )	$\mathbf{h}_{d,i} = \begin{bmatrix} 1 & & & & \\ & 1 & & & \\ & & \ddots & & \\ & & & & 1 \end{bmatrix}_{n_i \times n_i}$
First Order ( $d = 1$ )	$\mathbf{h}_{d,i} = \begin{bmatrix} 1 & -1 & & & \\ & 1 & -1 & & \\ & & \ddots & & \\ & & & & 1 & -1 \end{bmatrix}_{(n_i-1) \times n_i}$
Second Order ( $d = 2$ )	$\begin{bmatrix} 1 & -2 & 1 & & & \\ & 1 & -2 & \mathbf{h}_{d,i} = & & \\ & & \ddots & & & \\ & & & & 1 & -2 & 1 \end{bmatrix}_{(n_i-2) \times n_i}$

$$\varphi(\alpha) = \left| \|\mathbf{Y}^\sigma - \mathbf{T}\|^2 - \mathbf{M}\sigma^2 \right|. \quad [11]$$

Then, the selection of regularization parameter can be formulated as an optimization problem, in which the optimal regularization parameter,  $\alpha^*$ , is determined by minimizing the value of the objective function  $\varphi(\alpha)$ . That is,

$$\alpha^* = \arg \min \varphi(\alpha). \quad [12]$$

If the noise level  $\sigma$  of the observed temperature data is unknown, the L-curve criterion can be used to determine a suitable value for the regularization parameter. This criterion plots a curve of  $\{X, Y\} = \{\lg(\|\mathbf{Y}-\mathbf{T}\|), \lg(\|\mathbf{h}_d(\mathbf{q}^1, \mathbf{q}^2, \mathbf{q}^3 \dots)\|)\}$ , that typically has an ‘‘L’’ shape, with the optimal regularization parameter corresponding to the point of maximum curvature at the corner of the curve.<sup>[54,56]</sup> More information on methods for selecting regularization parameters can be found in classical literature.<sup>[51,52]</sup>

### 3. Solution procedure

Figure 2 shows the iteration process of the 2DIHCP algorithm. The first step is to make an initial guess for the heat flux,  $\mathbf{q}^j$ . Then, the temperatures corresponding to the thermocouple locations are calculated by solving the direct problem given by Eqs. [2b] through [2e] using  $\mathbf{q}^j$ . Next, solve the sensitivity coefficient problem given in Appendix A for the sensitivity coefficient matrix  $\mathbf{J}_j$  during the time from 0 to  $t_r$ . These calculated temperatures are then compared to the measured ones. If the stopping criteria given by Eqs. [8] through [10] are satisfied, the heat flux value is correct and the time step  $j$

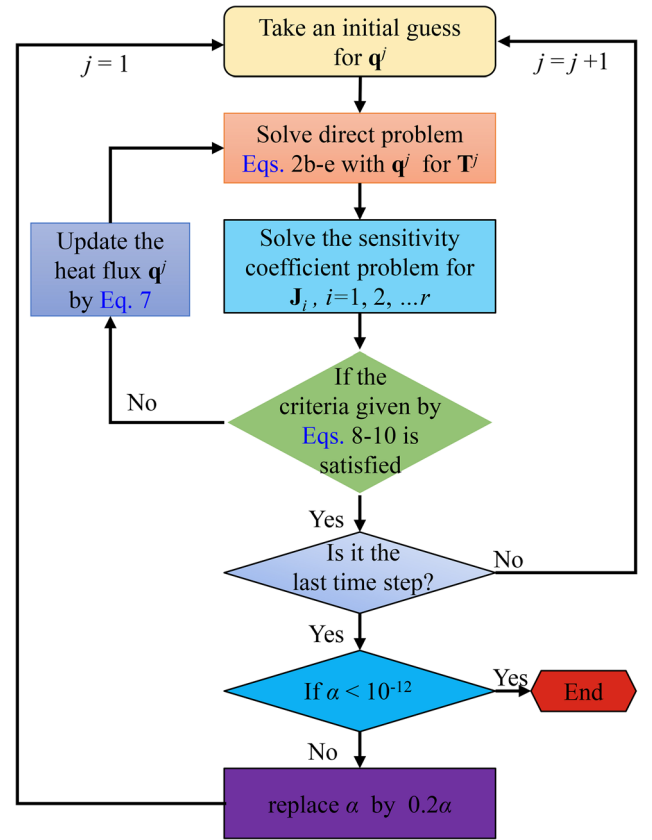


Fig. 2—Computational procedure of 2DIHCP algorithm.

increases to  $j+1$ , and the calculation for the next time step is conducted until the end of the time step. If the stopping criteria are not satisfied, the heat flux value  $\mathbf{q}^j$  is updated using Eq. [7], and substituted into the direct problem to calculate the responding temperatures until the stopping criteria are satisfied.

The partial differential equations (Eqs. [2b] through [2e] and Eqs. [A2a] through [A2d]) related to the 2DIHCP are solved using the finite difference method (FDM) with Crank–Nicolson (CN) semi-implicit scheme. The time steps must be at least as small as the time steps in the measured temperatures. It is practical to set the computational time step ( $\Delta t^*$ ) equal to  $1/N_f$  of the time interval for temperature sampling.<sup>[15]</sup>

$$\Delta t^* = \frac{\Delta t_{meas}^*}{N_f} = \frac{1}{f_s N_f}, \quad [13]$$

where  $f_s$  is the number of samples taken per second with the unit in Hz.  $\Delta t_{meas}$  is the time interval of temperature sampling.  $N_f$  is a positive integer and defaults to 1.

Prior to applying this method to inverse calculations, accuracy of FDM for solving partial differential equations was verified by the comparison of FDM numerical results to the analytical solution of a two-dimensional heat transfer problem from a textbook.<sup>[57]</sup> Additionally, it is worth noting that the sensitivity coefficient matrix can be computed only once if the sensitivity coefficient

problem is linear. Moreover, updating the heat flux  $\mathbf{q}^j$  using Eq. [2] only once might be sufficient in most cases to achieve accurate results.

### III. INFLUENCES OF THERMOCOUPLE PARAMETERS

This section is to verify the inverse problem model and investigate the impact of the depth of thermocouples beneath mold surface ( $w_1$ ), the temperature sampling rate ( $f_s$ ), and the noise level of temperature data ( $\sigma$ ), on the accuracy of heat flux estimations, aiming to provide recommendations for the thermocouple settings.

As shown in Figure 1, the direct problem in the test study involves the conduction of heat within a copper rectangular area labeled ABCD, with dimensions of  $0.021 \text{ m} \times 0.008 \text{ m}$  (height  $\times$  width) and an initial temperature of  $0 \text{ K}$ . The boundaries  $\Gamma_1$ ,  $\Gamma_3$ , and  $\Gamma_4$  are insulated. The validation and investigation process involves the following steps:

Firstly, specify the analytic expression for a pre-set heat flux  $g_{\text{exa}}(\Gamma_2, t)$  on the boundary  $\Gamma_2$ . It is general that the heat flux function containing a sharp corner poses the greatest difficulty for recovery by inverse analysis.<sup>[15]</sup> To assess the most stringent test conditions, we considered the heat flux involving a triangular variation in both time and space. That is,

$$g_{\text{exa}}(\Gamma_2, t^*) = A_0 f_1(y^*) f_2(t^*), \quad [14]$$

$$\text{with } f_1(y^*) = \begin{cases} \frac{y^* - l_1}{l_0}, & l_1 \leq y^* < l_2 \\ 1 - \frac{y^* - l_2}{l_0}, & l_2 \leq y^* \leq l_3, \text{ and } f_2(t^*) \\ 0, & \text{others.} \end{cases}$$

$$= \begin{cases} \frac{t^* - \tau_1}{\tau_1}, & \tau_1 \leq t^* < \tau_2 \\ 1 - \frac{t^* - \tau_2}{\tau_1}, & \tau_2 \leq t^* \leq \tau_3. \\ 0, & \text{others.} \end{cases}$$

where  $A_0$  is  $1 \times 10^6 \text{ W m}^{-2}$ ,  $l_0$ ,  $l_1$ ,  $l_2$ , and  $l_3$  are 0.007, 0.003, 0.010, and 0.017 m,  $\tau_1$ ,  $\tau_2$ , and  $\tau_3$  are 5, 10, and 15 seconds, respectively.

Secondly, set the location of temperature sensors in the computation domain. The location of temperature sensors in the computation domain is set as shown in Figure 1. The domain  $\Omega$  comprises two columns of  $2 \times 8$  thermocouples. The first column consists of eight virtual response thermocouples spaced 3 mm apart in the vertical direction and situated  $w_1$  beneath the mold hot surface. The second column comprises eight virtual thermocouples spaced 3 mm apart in the vertical direction and located on the boundary  $\Gamma_4$  (CD). Tests with different configuration of thermocouple parameters, including the depth of thermocouples beneath mold

**Table II. Configuration of Thermocouple for the Simulated Measurements**

Simulated Measured Temperature Data	Depth of Thermocouples Beneath Mold Surface ( $w_1$ )	Sampling Rate of Temperature ( $f_s$ )	Noise Level of Temperature Data ( $\sigma$ )
$W_1F_{010}N_{00}$	1	10	0
$W_3F_{010}N_{00}$	3	10	0
$W_5F_{010}N_{00}$	5	10	0
$W_3F_{005}N_{00}$	3	5	0
$W_3F_{030}N_{00}$	3	30	0
$W_3F_{060}N_{00}$	3	60	0
$W_3F_{100}N_{00}$	3	100	0
$W_3F_{010}N_{01}$	3	10	0.1 pct $Y_{\text{max}}$
$W_3F_{010}N_{05}$	3	10	0.5 pct $Y_{\text{max}}$
$W_3F_{010}N_{10}$	3	10	1.0 pct $Y_{\text{max}}$

$Y_{\text{max}}$  is the maximum measured temperature (K).

surface ( $w_1$ ), sampling rate of temperature ( $f_s$ ), and the temperature measurement error ( $\sigma$ ), are listed in Table II.

Thirdly, generate the simulated measured temperature data. Apply the pre-set heat flux  $g_{\text{exa}}(\Gamma_2, t)$  on the boundary  $\Gamma_2$ , run the direct problem given by Eqs. [2b] through [2e] to compute the temperatures using the FDM, while the sampling frequency of temperature is set as  $f_s$ . Then, Gaussian noise signals  $\sigma\omega$  ( $Y = Y_{\text{exa}} + \sigma\omega$ ,  $\sigma$  is the noise level of the observed temperature, and  $\omega$  is a random variable and will be within  $-2.576$  to  $2.576$  for the 99 pct confidence bounds) are added to the temperatures ( $Y_{\text{exa}}$ ) to mimic the thermocouple measurement error. Despite the absence of intentionally added noise to the data, it is worth noting that the calculated simulated temperature ( $W_1F_{010}N_{00}$ ,  $W_3F_{010}N_{00}$ , and  $W_5F_{010}N_{00}$ ) may not be perfectly precise. These calculated simulated temperature may still incorporate errors arising from the accumulation of finite difference method (FDM) rounding errors and truncation errors.<sup>[15,51]</sup>

Fourth, the reconstruction of heat flux by the IHCP. Substitute the simulated measured temperatures (Table II) into 2DIHCP for the heat flux ( $g_{\text{pred}}$ ) estimations. All the computations with  $17 \times 43$  discrete uniform grids are carried out by a computer with an Intel(R) Core (TM) i7-9700K CPU @ 3.60GHz and 32GB RAM memory.

Finally, evaluate the accuracy of the inverse analysis. The following relative error between the exact and the reconstructed result is employed to evaluate the accuracy of heat flux estimations:

$$e_{\text{pred}} = \frac{\|g_{\text{exa}}(\mathbf{x}, t) - g_{\text{pred}}(\mathbf{x}, t)\|}{\|g_{\text{exa}}(\mathbf{x}, t)\|} \times 100 \text{ pct}, \quad [15]$$

where  $g_{\text{exa}}$  and  $g_{\text{pred}}$  are the exact and the predicted heat fluxes, respectively. A high value of the relative error,  $e_{\text{pred}}$ , indicates that the reconstructed heat flux is of lower accuracy.

**Table III. Parameters Variation of Inverse Problem for Test Case**

Parameter	Variations
Number of Future Time Steps ( $r$ )	1, 2, 4, 6, 8, 10
Regularization Parameter ( $\alpha$ )	$10^{-9}$ , $10^{-8}$ , $10^{-7}$ , $10^{-6}$ , $10^{-5}$ , $10^{-4}$ , $5 \times 10^{-4}$ , $10^{-3}$ , $5 \times 10^{-3}$ , $10^{-2}$ , $5 \times 10^{-2}$ , $1 \times 10^{-1}$ , 1, 5, 10, 20, 30, 40, 50, 75, and 100
Order of Spatial Regularization ( $d$ )	zeroth, first, and second

In addition, the proposed 2DIHCP involves the selection of parameters, such as the number of future time steps ( $r$ ), the regularization parameter ( $\alpha$ ), and the order of spatial regularization ( $d$ ). These parameters have an impact on the accuracy of the 2DIHCP. Furthermore, the selection of optimal values for  $r$ ,  $\alpha$ , and  $d$  is interdependent with thermocouple errors.<sup>[16]</sup> As there is no established theory available to guide the simultaneous selection of optimal parameter values, a trial-and-error approach has commonly been employed to determine these three parameters. In this study, a total of 3780 distinct tests were conducted to determine these three parameters using the trial-and-error method. Each parameter ( $r$ ,  $\alpha$ ,  $d$ ) listed in Table III was individually tested, maintaining the other parameters at a constant value. The parameter ranges used are also outlined in this table.

#### A. Effect of Thermocouple Depth Beneath Mold Surface

The simulated temperature data used in 2DIHCP were acquired from thermocouples situated at varying depths ( $w_1$ ) below the mold surface ( $W_1F_{010}N_{00}$ ,  $W_3F_{010}N_{00}$ , and  $W_5F_{010}N_{00}$ ). As shown in Figure 3, a total of 1134 distinct tests were conducted. The accuracy of the inverse problem is quantified by the relative error ( $e_{\text{pred}}$ ), with the star  $\star$  symbol indicating the position of the minimum  $e_{\text{pred}}$ , which aligns with the optimal values of  $r$  and  $\alpha$ . Generally, any values of  $r$  and  $\alpha$  values that result in a relative error below 10.0 pct can be considered feasible solutions.<sup>[58]</sup> Notably, the absence of spatial regularization ( $\alpha$  is 0) yields a relative error ( $e_{\text{pred}}$ ) exceeding 10.0 pct. The optimal range for  $r$  is 1 to 2, while the optimal range for  $\alpha$  is  $10^{-7}$  to  $10^{-4}$ , which is consistent with the previous studies.<sup>[15,16]</sup>

As the depth of thermocouples beneath mold surface ( $w_1$ ) increases, the optimal number of future time steps ( $r$ ) should be raised to uphold the accuracy of the inverse problem. For example, the optimal  $r$  is 1 and 2 for thermocouples located 3 and 5 mm beneath the mold surface, respectively. Increasing the optimal  $r$  when  $w_1$  increases from 3 to 5 mm resulted in an increase in the required CPU time. Specifically, the required CPU time increased from 2.20 to 3.22 seconds for zeroth-order spatial regularization, from 2.01 to 3.30 seconds for first-order spatial regularization, and from 1.96 to 3.22 seconds for second-order spatial regularization.

Figure 4 shows the minimum  $e_{\text{pred}}$  and the respective required computing time (CPU time) for heat flux reconstructions by the inverse analysis. It could be observed that the accuracy of heat flux estimations reduces with increasing the depth of thermocouples below the surface. Using first-order spatial regularization, the minimum  $e_{\text{pred}}$  for estimating heat flux is 6.48, 6.58, and 8.47 pct for thermocouples located 1, 3, and 5 mm beneath the mold surface, respectively. The reduction in accuracy is 1.54 pct when the depth of thermocouples beneath mold surface ( $w_1$ ) increases from 1 to 3 mm. However, the accuracy reduction is 26.92 to 31.21 pct when  $w_1$  increases from 3 to 5 mm. This trend is similar to that observed with zeroth- and second-order spatial regularizations. The results suggest that to accurately detect mold heat flux, the depth of thermocouples beneath mold surface should not exceed 3 mm.

In the context of a semi-infinite solid ( $0 < x < \infty$ ) initially at the temperature of  $T_0$ , the situation involves a boundary surface at  $x = 0$  exposed to a spatially constant heat flux with temporal oscillations as  $q(t) = A_q \cos(2\pi ft)$ , where  $A_q$  and  $f$  are the amplitude and frequency of oscillations for the heat flux, respectively. Following the attenuation of transient effects, the quasi-stationary temperature distribution in the solid can be described using the analytical solution,<sup>[21]</sup>

$$T(x, t) = T_0 + \frac{A_q}{\lambda} \sqrt{\frac{\lambda}{2\pi f \rho c}} \exp\left(-x \sqrt{\frac{\pi f \rho c}{\lambda}}\right) \cos\left(2\pi ft - x \sqrt{\frac{\pi f \rho c}{\lambda}} - \frac{\pi}{4}\right). \quad [16]$$

The oscillation amplitude for the temperature at any location is

$$A_T = \frac{A_q}{\lambda} \sqrt{\frac{\lambda}{2\pi f \rho c}} \exp\left(-x \sqrt{\frac{\pi f \rho c}{\lambda}}\right). \quad [17]$$

From Eq. [17], it is evident that the oscillation amplitude of temperature in the solid decreases exponentially as depth below the surface increases. To precisely estimate the boundary heat flux, it must place a temperature sensor at a depth where the temperature oscillation amplitude significantly exceeds the measurement error. Otherwise, it is impossible to distinguish if the measured temperature oscillation is due to changes in the boundary heat flux or due to measurement errors.<sup>[15,21]</sup> Generally, sensor measurement errors ( $\sigma$ ) are provided, or simulated temperature measurement data obtained through the finite difference method (FDM) might not be perfectly accurate. Consequently, the information content ( $A_T/\sigma$ ) of the temperature measurement in the solid decreases as the depth of the sensor below the surface increases. This factor contributes to decreased accuracy in heat flux estimations as the depth of the thermocouple beneath the mold surface increases.

In general, first-order spatial regularization provides higher accuracy for heat flux reconstruction than both zeroth- and second-order spatial regularizations. For instance, when zeroth-order spatial regularization is utilized, the minimum  $e_{\text{pred}}$  is 6.61, 6.60, and 8.66 pct for



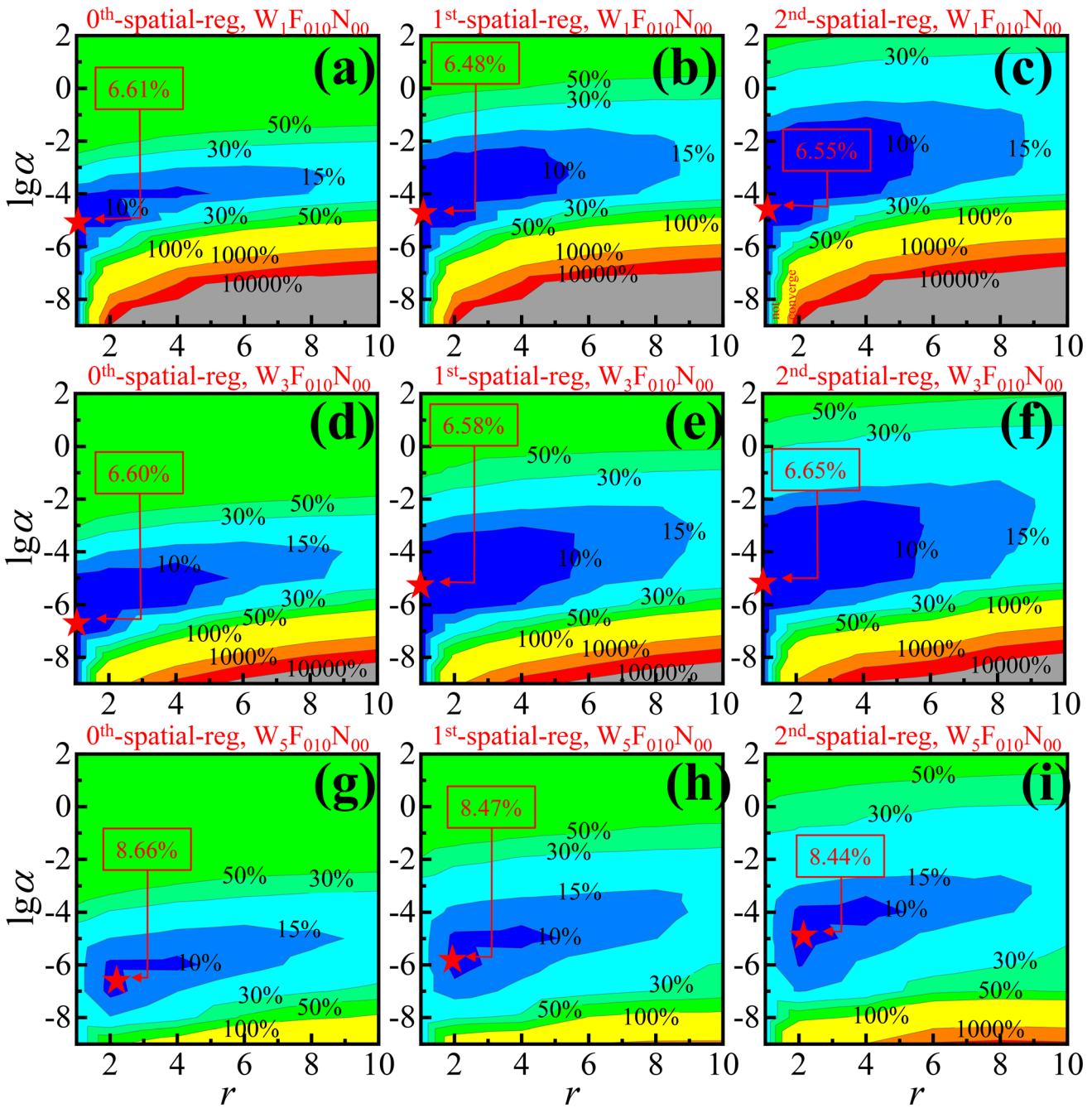


Fig. 3—Effects of the depth of thermocouples beneath mold surface ( $w_1$ ) and the order of spatial regularization on the relative error ( $e_{\text{pred}}$ ): (a), (b), and (c)  $w_1$  is 1 mm; (d), (e), and (f)  $w_1$  is 3 mm; and (g), (h), and (i)  $w_1$  is 5 mm. ★ denotes the location of minimum  $e_{\text{pred}}$ .

thermocouples located 1, 3, and 5 mm beneath the mold surface, respectively. Meanwhile, the corresponding values for the first-order spatial regularization are 6.48, 6.58, and 8.47 pct, and those for the second-order spatial regularization are 6.55, 6.65, and 8.44 pct.

Figure 5 shows heat fluxes at  $y = 10.5$  mm (a) and at  $t = 10$  s (b) reconstructed using different depths of thermocouples beneath the mold surface ( $w_1$ ). The optimal values of  $r$  and  $\alpha$  for these estimations correspond to the location of minimum  $e_{\text{pred}}$  (represented by

a star) in Figure 3. As shown in Figure 5(a), the predicted heat fluxes match the exact one, except for a slight deviation at 10.5 seconds when the exact heat flux exhibits a sharp spatial change, indicating that the temporal accuracy of the inverse results is roughly satisfactory. However, the recovered heat fluxes deviate from the exact value when the exact heat flux undergoes a sharp spatial change at locations where  $y^*$  is 3, 10, and 17 mm, suggesting that the spatial accuracy of the inversion results is inadequate, as seen in Figure 5(b).

This could be attributed to the fact that a sharply changing heat flux is not differentiable, especially because the spatial regularization term in the inverse problem (Eq. [2]) limits the sharp spatial changes of the reconstructed heat flux.

In summary, it is observed that the accuracy of heat flux estimations using 2DIHCP decreases as the depth of thermocouples beneath mold surface increases, and it is recommended that the depth should not exceed 3 mm. The optimal number of future time steps ( $r$ ) should also be increased as the locations of temperature measurements get further away from the mold surface, which increases the required CPU time.

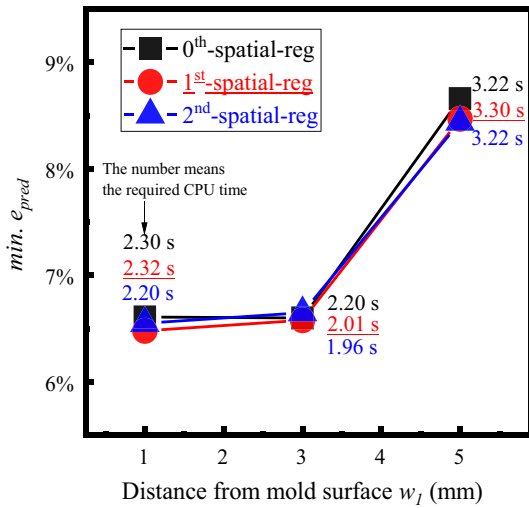


Fig. 4—Changes of the relative error ( $e_{pred}$ ) and required CPU time with the depth of thermocouples beneath mold surface ( $w_1$ ).

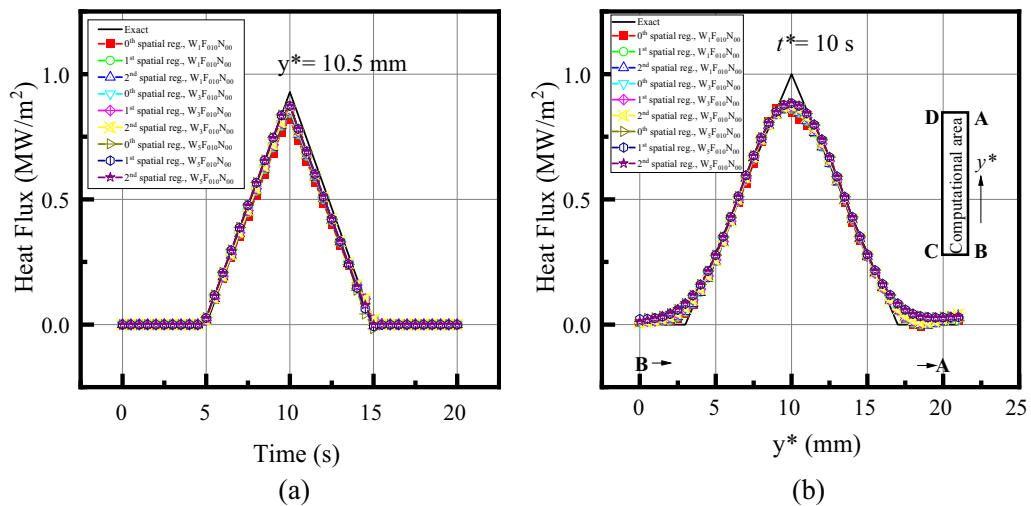


Fig. 5—Comparison of heat fluxes reconstructed with different orders of spatial regularization and depth of thermocouples beneath mold surface ( $w_1$ ): (a) heat fluxes at  $y = 10.5$  mm and (b) heat fluxes at the time of 10 seconds.

## B. Effect of Temperature Sampling Rate

The simulated temperature data were acquired from thermocouples with five different temperature sampling frequencies ( $W_3F_{005}N_{00}$ ,  $W_3F_{010}N_{00}$ ,  $W_3F_{030}N_{00}$ ,  $W_3F_{060}N_{00}$ , and  $W_3F_{100}N_{00}$ ). In Figure 6, 1512 distinct tests were conducted. The accuracy of the inverse problem is characterized by the relative error ( $e_{pred}$ ), and the star  $\star$  denotes the location of minimum  $e_{pred}$  corresponding to the optimal values of  $r$  and  $\alpha$ . The absence of spatial regularization ( $\alpha$  is 0) also leads to a relative error ( $e_{pred}$ ) exceeding 10.0 pct. The optimal  $r$  increases from 1 to 10 as the temperature sampling frequency increases from 0 to 100 Hz, while the optimal range for  $\alpha$  is  $10^{-6}$  to  $10^{-4}$ .

The minimum  $e_{pred}$  and the respective CPU time of heat flux estimations by the inverse analysis are presented in Figure 7. The accuracy of heat flux estimations decreases as the temperature sampling rate ( $f_s$ ) increases from 5 to 10 Hz, but then remains stable at around 6.80 pct when  $f_s$  increased from 10 to 60 Hz, and finally increases from 6.80 to 8.60 pct when  $f_s$  increased from 60 to 100 Hz.

When zeroth-order spatial regularization is employed, the minimum  $e_{pred}$  of predicting heat flux is 9.38, 6.60, 6.97, 7.03, and 8.69 pct for the sampling rate of 5, 10, 30, 60, and 100 Hz, respectively. Meanwhile, the corresponding value for first-order spatial regularization are 9.38, 6.58, 6.56, 6.80, and 8.53 pct, and those for the second-order spatial regularization are 9.42, 6.65, 6.62, 6.87, and 8.51 pct. It is indicated that first- and second-order spatial regularizations appear to be more accurate than zeroth-order spatial regularization when the sampling rate is high.

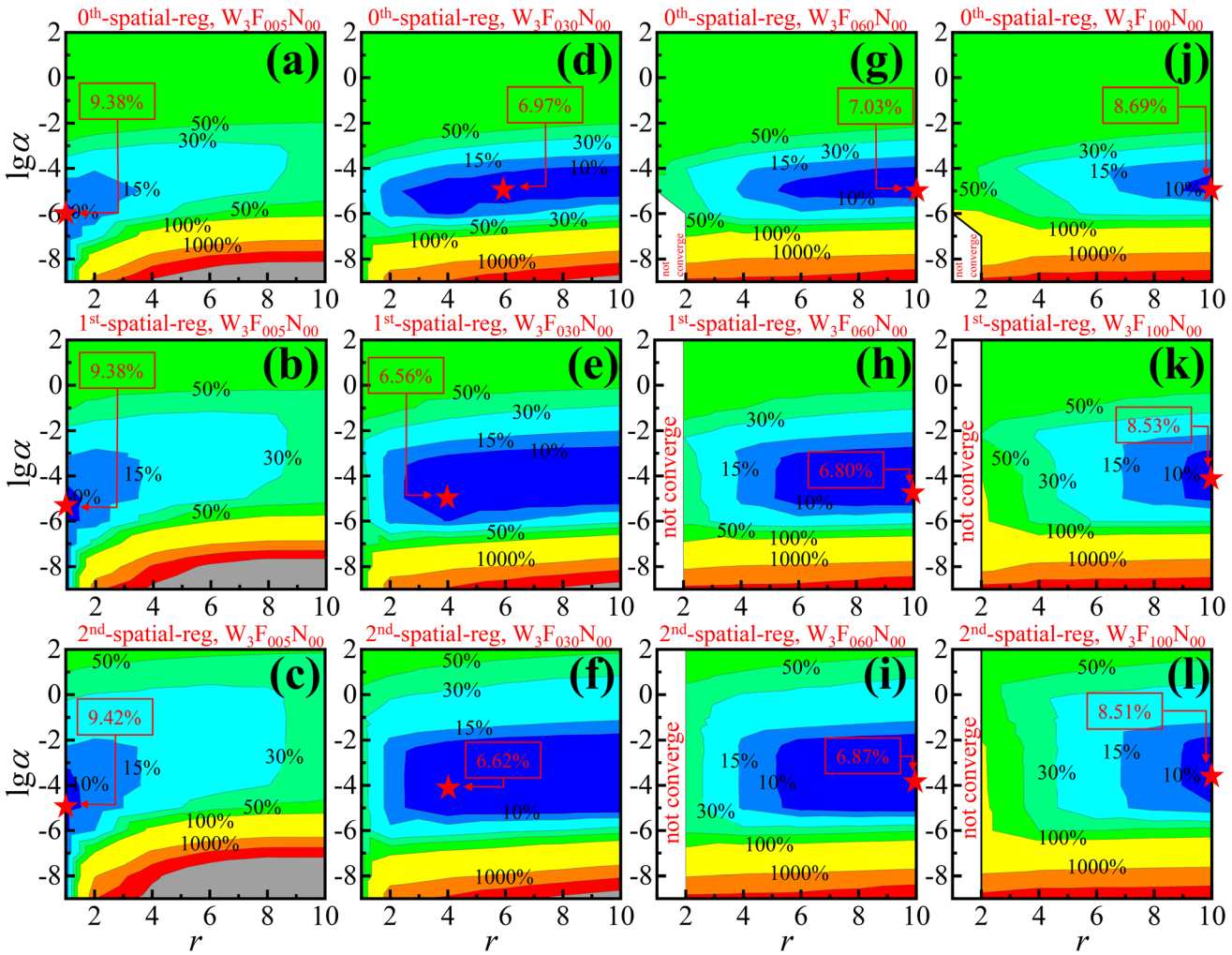


Fig. 6—Effects of temperature sampling rate ( $f_s$ ) and order of spatial regularization on the relative error ( $e_{\text{pred}}$ ): (a), (b), and (c)  $f_s$  is 5 Hz, (d), (e), and (f)  $f_s$  is 30 Hz, (g), (h), and (i)  $f_s$  is 60 Hz, and (j), (k), and (l)  $f_s$  is 100 Hz. ★ denotes the location of minimum  $e_{\text{pred}}$ .

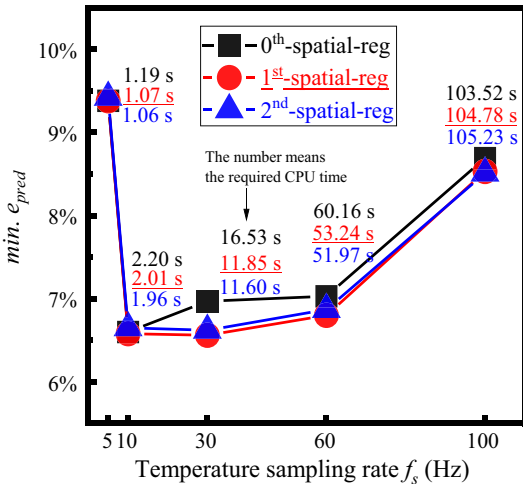


Fig. 7—Effects of the depth of thermocouples beneath mold surface ( $w_1$ ) and order of spatial regularization on the relative error ( $e_{\text{pred}}$ ).

The time step is a crucial factor in the inverse heat conduction problem. Beck<sup>[15]</sup> and Blanc<sup>[16]</sup> *et al.* observed that the sampling rate affects the magnitude of the sensitivity coefficient ( $\mathbf{J}$ ) by influencing the time step used to solve the sensitivity coefficient problem. This, in turn, affects the stability of the algorithm (Eq. [7]) for solving the inverse problem. Instability of the inverse problem refers to the high sensitivity of the solution to small changes in the input data's noise, which can lead to substantial errors in the output. A semi-empirical criterion<sup>[15,16]</sup> ensuring stability in the heat flux estimator, as expressed in Eq. [7], is that the dimensionless time step should exceed a critical value.

$$\Delta t = \frac{\lambda \Delta t^*}{\rho c e^2} > \Delta t_{\text{cri}}, \quad [18]$$

where  $e$  is the maximum distance between the sensors and the point where the heat flux is evaluated. The critical value, denoted as  $\Delta t_{\text{cri}}$ , ranges from 0.005 to 0.01, depends upon factors such as the number of

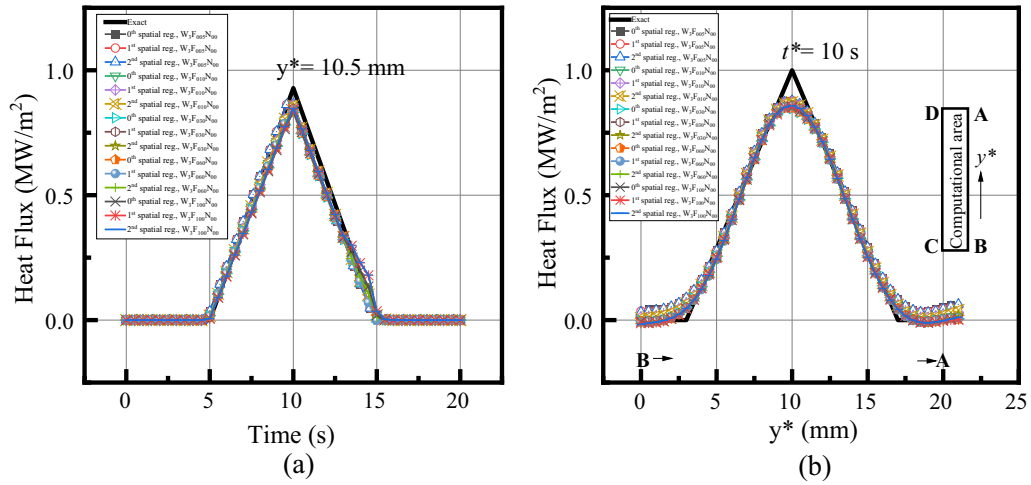


Fig. 8—Comparison of the heat fluxes reconstructed with different orders of spatial regularization and temperature sampling rate ( $f_s$ ): (a) heat fluxes at  $y = 10.5$  mm, and (b) heat fluxes at the time of 10 seconds.

spatial dimensions in the heat transfer scenario, the sensor’s depth, and the solid’s temperature diffusivity. In this investigation, we adopt a value of 0.005 for  $\Delta t_{\text{cri}}$ .

The dimensionless time steps employed in the 2DIHCP are 0.0521, 0.0261, 0.0087, 0.0043, and 0.0026 for the sampling rates of 5, 10, 30, 60, and 100 Hz, respectively. As the temperature sampling frequency increases, the dimensionless time step decreases, which may lead to potential instability in the 2DIHCP. At a sampling rate of 60 Hz, the minimal  $e_{\text{pred}}$  of predicting heat flux ranges from 6.80 to 7.03 pct, which is slightly higher than the values of 6.58 to 6.97 pct observed at a 30 Hz sampling rate. With dimensionless time steps of 0.0043 and 0.0026 for 60 Hz and 100 Hz sampling rates, respectively, both fall below the critical value of 0.005, indicating instability in the 2DIHCP. This instability could lead to a reduction in accuracy for inverse prediction.

Although the dimensionless time step of 0.0521 is larger than the critical value of 0.005, indicating stability in the 2DIHCP, its accuracy remains poor at a sampling rate of 5 Hz. Then, a speculation would be made that if the temperature is measured too slowly, the heat transfer process may have already changed. Such discrepancies between observed and true temperatures can result in inaccuracies in measurements.

A noticeable improvement in the accuracy of the inverse problem is observed at sampling frequencies ( $f_s$ ) is 10, and 30 Hz. A sufficiently high sampling rate allows for the thorough capture of temperature fluctuations, thereby enhancing the accuracy of inverse problem. Secondly, the dimensionless time steps utilized in the 2DIHCP, namely 0.0261 and 0.0087 for 10 Hz and 30 Hz sampling rates, respectively, exceed the critical value of 0.005. These combined factors contribute to a reasonably accurate solution for the inverse problem.

It could be observed that the required CPU time increases significantly as the temperature sampling rate increases due to the optimal  $r$  increases, but the effect of

the order of spatial regularization on the CPU time is not significant. For example, when zeroth-order spatial regularization is employed, the CPU time of predicting heat flux is 1.19, 2.20, 16.53, 60.16, and 103.52 seconds for the sampling rate of 5, 10, 30, 60, and 100 Hz, respectively. While the corresponding values for first-order and second-order spatial regularization are similar.

Figure 8 displays heat fluxes at  $y = 10.5$  mm (a) and at  $t = 10$  s (b) reconstructed using temperature measurements with various sampling rates ( $f_s$ ). The 2DIHCP calculations utilized the optimal  $r$  and  $\alpha$  that corresponded to the location of minimum  $e_{\text{pred}}$  (★) in Figure 6. As shown in Figure 8(a), the predicted heat fluxes match the exact one, except for a slight deviation at 10.5 seconds when the exact heat flux exhibits a sharp spatial change. This suggests that the temporal accuracy of the inversion results is roughly satisfactory. Conversely, the recovered heat fluxes may deviate from the exact value when the exact heat flux exhibits a sharp spatial change at certain locations, such as  $y^* = 3, 10,$  and  $17$  mm in Figure 8(b). This indicates that the spatial accuracy of the inversion results is inadequate. The inadequate accuracy may be due to the fact that a sharply changing heat flux is not differentiable. In particular, the spatial regularization term in the inverse problem (Eq. [2]) limits the sharp spatial changes of the reconstructed heat flux.

In brief, it is observed that the accuracy of the heat flux initially increases when the temperature sampling rate ( $f_s$ ) increases from 5 to 10 Hz, then remains at a relatively stable values when  $f_s$  increases from 10 to 60 Hz, and finally decreases when  $f_s$  increases from 60 to 100 Hz. Additionally, both first- and second-order spatial regularizations appear to be more accurate than zeroth-order spatial regularization when using high-temperature sampling rates. However, increasing the temperature sampling rate significantly increases the required CPU time. While the effect of the order of spatial regularization on the CPU time is not apparent.

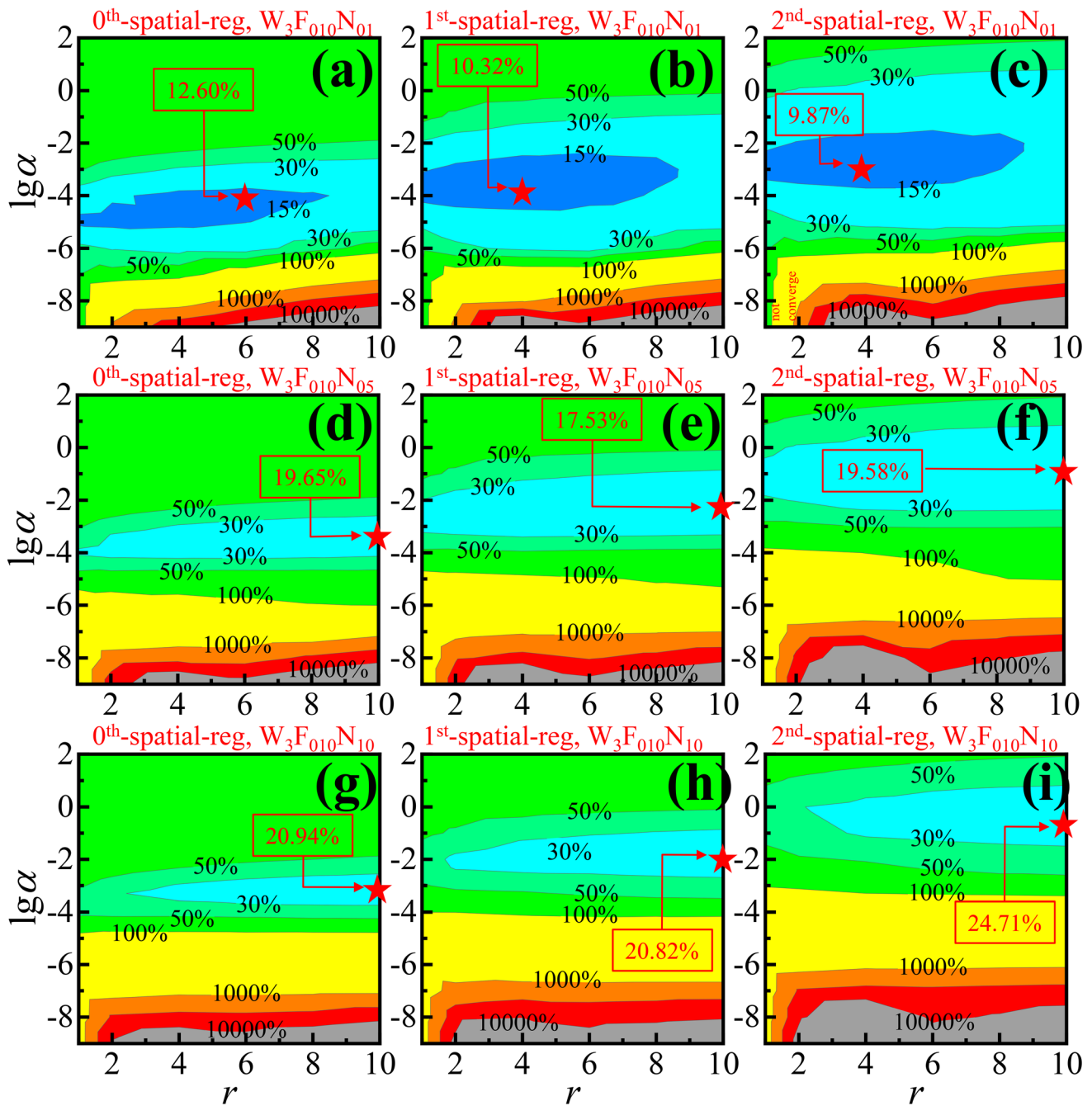


Fig. 9—Effects of temperature measuring noise ( $\sigma$ ) and order of spatial regularization on the relative error ( $e_{\text{pred}}$ ): (a), (b), and (c)  $\sigma = 0.1$  pct  $Y_{\text{max}}$ , (d), (e), and (f)  $\sigma = 0.5$  pct  $Y_{\text{max}}$ , and (g), (h), and (i)  $\sigma = 1.0$  pct  $Y_{\text{max}}$ . ★ denotes the location of minimum  $e_{\text{pred}}$ .

### C. Effect of Measurement Noise

The simulated temperature data used in 2DIHCP were acquired from thermocouples with four different noise levels of temperature measurement ( $W_3F_{010}N_{00}$ ,  $W_3F_{010}N_{01}$ ,  $W_3F_{010}N_{05}$ , and  $W_3F_{010}N_{10}$ ). As shown in Figure 9, 1134 distinct tests were conducted, the accuracy of the inverse problem is characterized by the relative error ( $e_{\text{pred}}$ ), and star ★ denotes the location of minimum  $e_{\text{pred}}$  corresponding to the optimal values of  $r$  and  $\alpha$ . The absence of spatial regularization ( $\alpha$  is 0) also leads to a relative error ( $e_{\text{pred}}$ ) exceeding 10.0 pct. The

optimal  $r$  increases from 4 to 10 as the noise level increases from 0.1 pct  $Y_{\text{max}}$  to 0.5 pct  $Y_{\text{max}}$ , while the optimal range for  $\alpha$  is  $10^{-4}$  to 0.5.

To ensure the accuracy, the optimal number of future time steps ( $r$ ) should be increased as the measurement error increases. For example, the optimal  $r$  is 1, 4, 10, and 10 for measurement errors of 0, 0.1 pct  $Y_{\text{max}}$ , 0.5 pct  $Y_{\text{max}}$ , and 1.0 pct  $Y_{\text{max}}$ , respectively. As results of increasing  $r$ , the required CPU time required for inverse analysis also increases. The corresponding required computing time (CPU time) is 2.01, 5.97, 15.85, and 20.17 seconds. When the temperature measurement is

noise free, the minimum  $e_{\text{pred}}$  is 6.60, 6.58, and 6.65 pct for the zeroth-, first-, and second-order spatial regularizations, respectively. Meanwhile, the corresponding values are 19.65, 17.53, and 19.58 pct when the measurement error is 0.5 pct  $Y_{\text{max}}$ . It suggests that first-order spatial regularization is more accurate than both zeroth- and second-order spatial regularizations when the temperature measurement contains errors.

The minimum  $e_{\text{pred}}$  and the respective CPU time of heat flux estimations by the inverse analysis are presented in Figure 10. It could be observed that the accuracy of heat flux estimations decreases as the temperature measurement error increases (Figure 10). For example, when first-order spatial regularization is used, the minimum  $e_{\text{pred}}$  of heat flux estimations is 6.58,

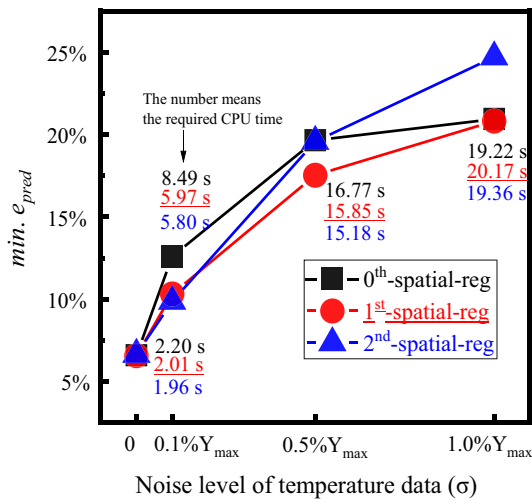


Fig. 10—Changes of the relative error ( $e_{\text{pred}}$ ) and CPU time required with noise level of temperature measurement.

10.32, 17.53, and 20.82 pct for measurement errors of 0, 0.1 pct  $Y_{\text{max}}$ , 0.5 pct  $Y_{\text{max}}$ , and 1.0 pct  $Y_{\text{max}}$ , respectively. It is easy to notice from Eq. [17] that at a specific location with a certain depth beneath the mold surface, the information content ( $A_T/\sigma$ ) concerning temperature variation decreases as the noise level in temperature measurements rises. Consequently, the accuracy of the 2DIHCP decreases as the noise level in temperature measurements increases.

Figure 11 presents heat fluxes at  $y = 10.5$  mm (a) and  $t = 10$  s (b) reconstructed using temperatures with varying levels of measurement error ( $\sigma$ ). The optimal  $r$  and  $\alpha$  for heat flux estimation correspond to the location of minimum  $e_{\text{pred}}$  (★) in Figure 9. The recovered heat flux deviates from the exact value at  $y^* = 3, 10,$  and  $17$  mm (a) and at  $10.5$  seconds (b) when the exact heat flux exhibits sharp spatial changes. Additionally, increasing measurement error results in decreased temporal accuracy of the heat fluxes, while spatial accuracy decreases significantly. The inverse analysis accuracy decreases with increasing temperature measurement error, which is consistent with the findings from Figure 10. This may be due to the fact that a sharply changing heat flux is not differentiable, particularly because the spatial regularization term in the inverse problem (Eq. [2]) limits sharp spatial changes in the reconstructed heat flux. This finding is consistent with those from Figures 5 and 8.

To sum up, it is observed that the accuracy in inverse analysis decreases with increasing temperature measurement error. To improve the accuracy, increasing the number of future time steps ( $r$ ) is necessary but requires longer computing time. First-order spatial regularization is more accurate than both zeroth- and second-order spatial regularizations when the temperature measurement contains errors.

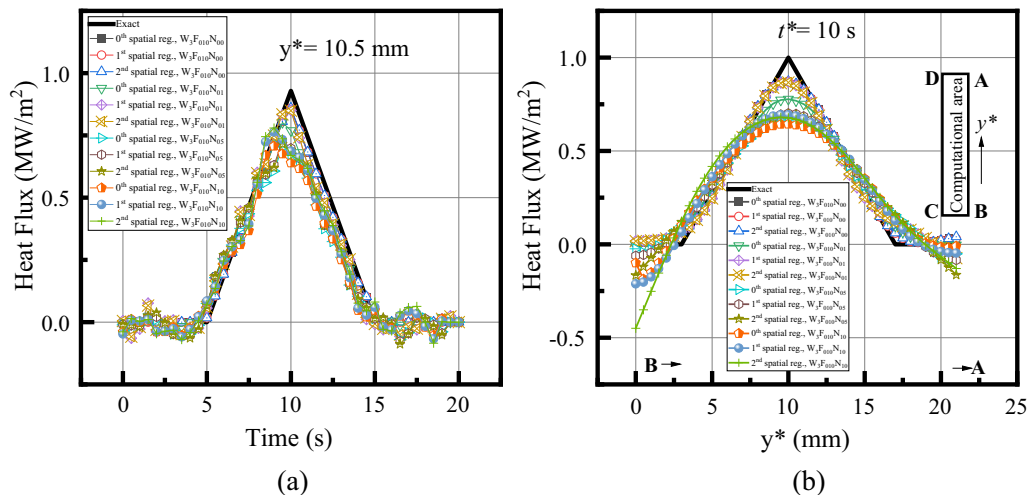


Fig. 11—Comparison of the heat fluxes reconstructed using the temperatures with different noise levels (0, 0.1 pct  $Y_{\text{max}}$ , 0.5 pct  $Y_{\text{max}}$ , and 1.0 pct  $Y_{\text{max}}$ ): (a) heat fluxes at  $y = 10.5$  mm, and (b) heat fluxes at the time of 10 seconds.

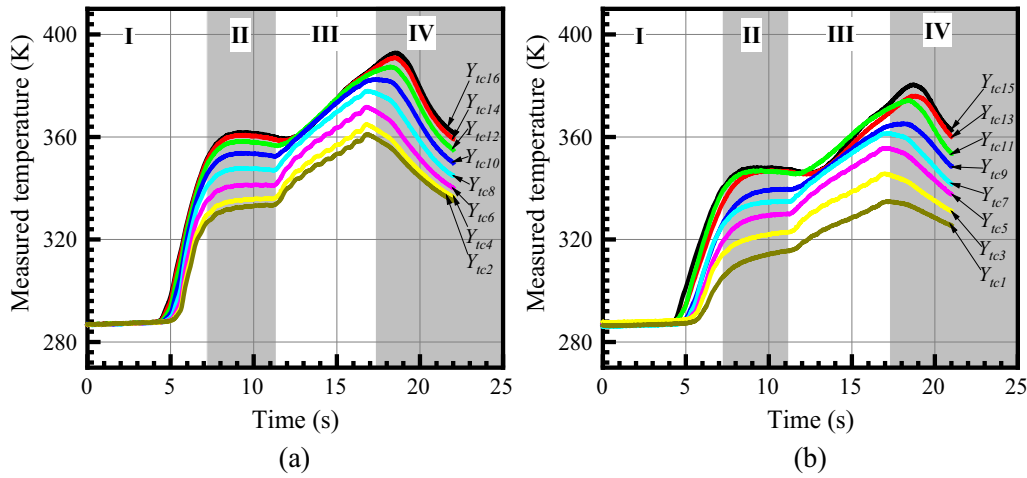


Fig. 12—Measured mold wall temperatures during the experiment: (a) Temperature of first column of thermocouples, and (b) Temperature of second column of thermocouples.

#### IV. APPLICATION TO A CASTING EXPERIMENT

The casting experiment was carried out using a mold simulator apparatus. During the casting experiments, the mold oscillation frequency was 1.67 Hz, the oscillation stroke was 6.0 mm, the pouring temperature was 1782 K, the casting speed was 0.6 m/min, the flow rate of the mold cooling water was 7.5 L/min, mold temperatures sampling rate was 60 Hz, and a standard deviation of thermocouple measurements  $\sigma$  is 0.5 K.

Figure 12 shows the temperature history of the thermocouples located inside the mold (as listed in Figure 1) during the experiment. The first column of thermocouples (3 mm away from the mold's hot surface) had temperatures that were 11.3 K to 26.6 K higher than the second column of thermocouples (8 mm away from the mold's hot surface) during the casting. The measured mold temperatures can be divided into four stages based on the casting process. At stage I (0 to 7.1 seconds), the responding temperatures rapidly rise the mold and extractor, initially at room temperature, were submerged into the molten steel. At stage II (7.1 to 11.8 seconds), temperatures continued to rise before stepping into a relative steady state as the mold and extractor were held for a few seconds, allowing for the solidification of a shell normal to the mold external surface. The thermal resistance between the mold and the liquid steel increased due to the growth of the initial solidifying steel shell and the infiltration and crystallization of the slag film between the mold and shell, as well as the formation of interfacial thermal resistance between the mold and slag film.<sup>[12,30,59,60]</sup> Stage III (11.8 to 16.6 seconds) corresponds to continuous casting, where the liquid steel level was at 16.5 mm in the y-axis. In this stage, temperatures increased as the solidified shell was withdrawn downward by the extractor and the fresh liquid melt continuously heated the mold. During stage IV, the mold and extractor, along with the attached steel shell, were removed from the melt and

cooled to room temperature. The responding temperatures continued to increase and then decrease as the mold was drawn out of the bath.

##### A. Choice of Sequential Regularization Method parameters

In this section, a methodology that combines the L-curve technique with Morozov's criterion is used to determine the regularization parameter ( $\alpha$ ). This approach is motivated by the unexpected results observed in inverse problems involving first- and second-order spatial regularizations and the L-curve method. When the optimal  $\alpha$  is determined using the L-curve method, the reconstructed heat flux shows limited spatial variation for the first-order spatial regularization method. In contrast, the reconstructed heat flux appears messy for the second-order spatial regularization method.

To explore this phenomenon, Figure 13 shows L-curve plots of inverse calculations with different orders of spatial regularization and numbers of future time steps ( $r$ ). Increasing  $\alpha$  leads to greater filtering of the heat flux, resulting in a smoother heat flux with minimal changes. Conversely, smaller values of  $\alpha$  lead to an unstable heat flux that exhibits oscillatory behavior. For the L-curve criterion, the optimal value of  $\alpha$  is located at the left corner of the curve, where heat flux fluctuations are suppressed, and  $\lg(\|\mathbf{h}_d(\mathbf{q}^1, \mathbf{q}^2, \mathbf{q}^3 \dots)\|)$  begins to stabilize as  $\alpha$  increases. The intermediate horizontal segment of the L-curve corresponds to a relatively stable value of  $\lg(\|\mathbf{h}_d(\mathbf{q}^1, \mathbf{q}^2, \mathbf{q}^3 \dots)\|)$  as  $\alpha$  varies, indicating that the heat flux reaches a state of stability. Figure 13(a) shows L-curve for zeroth-order spatial regularization, an  $\alpha$  exists that satisfies Morozov's criterion within the intermediate horizontal segment of the L-curve. This indicates that the heat flux stability can be reconstructed using zeroth-order spatial regularization, and meanwhile the  $\alpha$  value can be accepted.

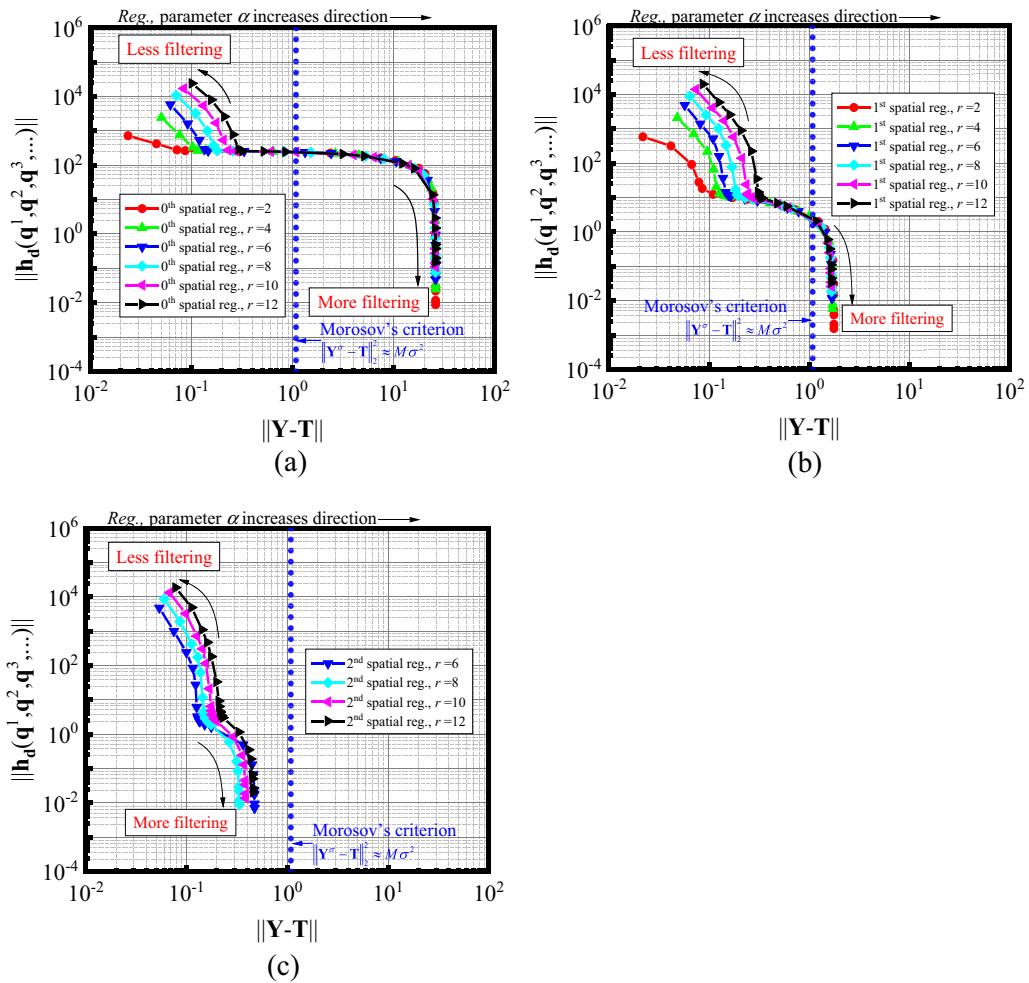


Fig. 13—L-curve of the inverse calculations with different number of future time steps ( $r$ ): (a) zeroth-, (b) first- and (c) second-order spatial regularizations. ‘More filtering’ denotes the heat flux stays very smooth, and only changes a little when a larger  $\alpha$  is used. ‘Less filtering’ denotes the heat flux exhibits oscillatory behavior and become unstable when a small  $\alpha$  is utilized.

Figure 13(b) shows L-curve for first-order spatial regularization, an  $\alpha$  exists that satisfies Morozov’s criterion within the “more filtering” segment of the L-curve. This indicates that the reconstructed heat flux has limited spatial variation and undergoes more filtering. In Figure 13(c), the L-curve is located to the left of Morozov’s criterion, indicating that the second-order spatial regularization method may result in overfitting of observed temperatures. This can cause perturbations in the heat flux. Therefore, first- and second-order spatial regularizations are not suitable for mold heat flux estimation.

As a result, zeroth-order spatial regularization is employed to estimate the heat flux for the mold simulator runs. According to Figure 13(a), the optimal value of  $\alpha$  is  $7.32 \times 10^{-5}$ , which corresponds to the intersection of the intermediate horizontal segment of the L-curve and Morozov’s criterion. According to the studies by Beck<sup>[15]</sup> and Blanc,<sup>[16]</sup> the number of future time steps ( $r$ ) is set to 6. The heat flux reconstruction process for a mold simulator experiment takes  $2.56 \pm 0.05$  seconds of CPU time, which is only 8.84 pct of the

experiment’s total duration of 29 seconds. This indicates that the proposed 2DIHCP method is suitable for online monitoring of mold heat flux.

## B. Heat Fluxes Near the Meniscus Area

### 1. The reconstructed mold heat flux

In Figure 14(a), the mold surface heat fluxes reconstructed by 2DIHCP using the measured temperatures during mold simulator experiment are presented. The heat fluxes selected from the mold hot surface (Line AB in Figure 1) can be divided into four stages based on the casting process. During Stage I (0 to 7.1 seconds), as the assembly of the mold and the extractor submerge into the molten steel, the heat fluxes rapidly increase, reaching their peak value when the liquid contacts the mold. As it enters Stage II (7.1 to 11.8 seconds), the oscillating mold and extractor are held for a few seconds to allow the shell to solidify normal to the external surface of the mold. This results in a reduction of the mold heat fluxes due to the increased thermal resistance between the mold and melt, caused by the growth of the



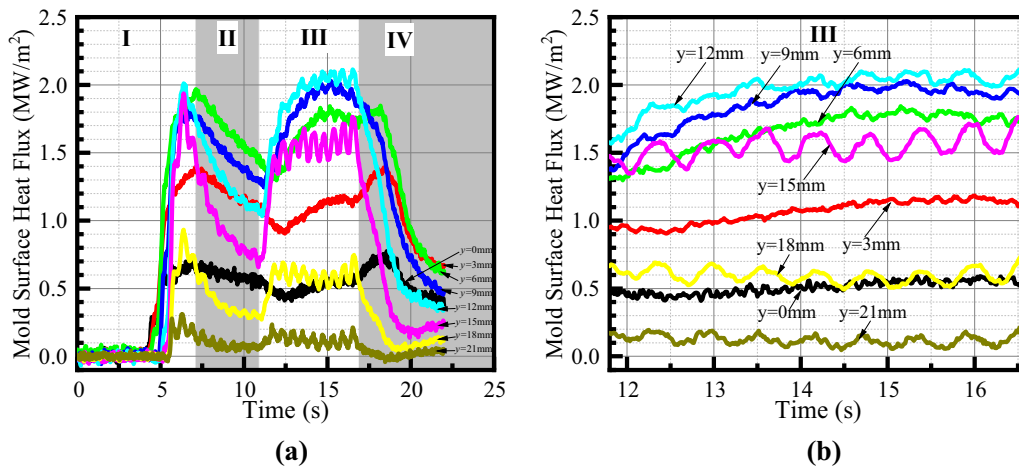


Fig. 14—Heat fluxes of the selected positions calculated by 2DIHCP: (a) heat flux during experiment, and (b) heat flux during the period of continuous casting at stage III.

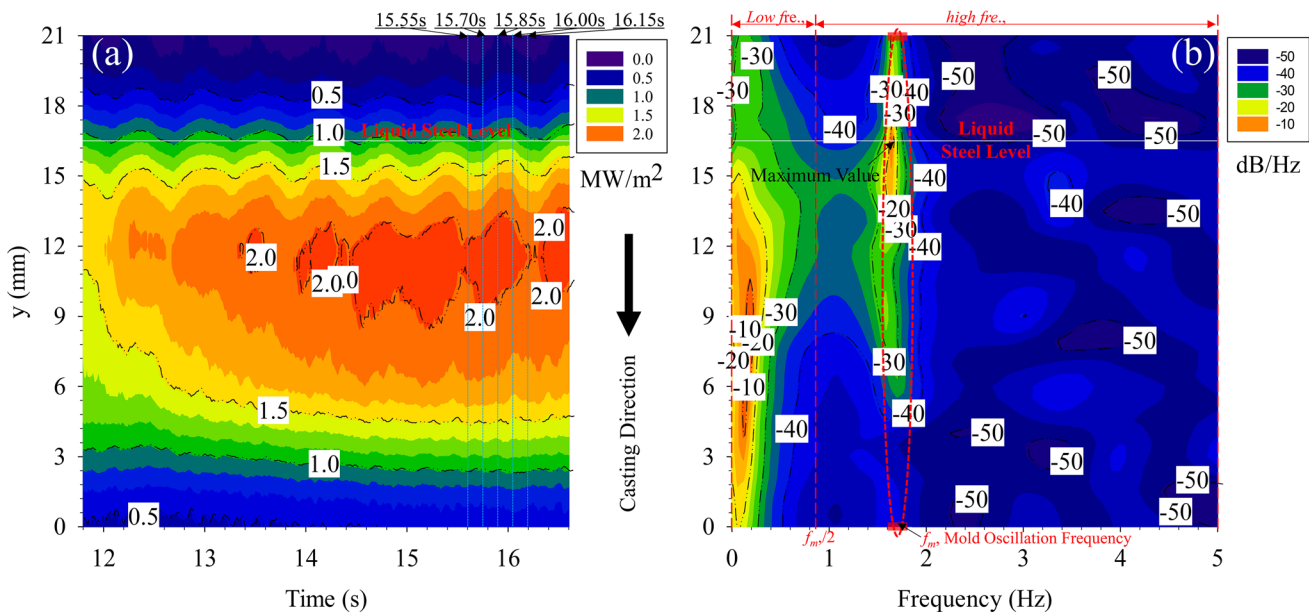


Fig. 15—(a) Recovered mold heat flux the period of continuous casting at stage III: Heat flux, and (b) PSD analysis for the heat flux at stage III.

initial solidifying steel shell, infiltration and crystallization of the slag film between the mold and shell, and the formation of interfacial thermal resistance between the mold and slag film.<sup>[12,30,59–61]</sup> In Stage III (11.8 to 16.6 seconds), the liquid steel level corresponds to 16.5 mm in the  $y$ -axis. When the solidifying shell is withdrawn, the heat fluxes begin to rise as fresh liquid melt comes in contact with the mold, heating it up. The heat flux reaches a quasi-steady state (Figure 14(b)) as the meniscus area of the molten steel is continuously cast downward and fresh molten steel is continuously filling the meniscus. The variation of the heat fluxes during continuous casting can be clearly observed in the region of the liquid steel level, and this is due to the oscillation of the mold in and out of the bath, as explained in the previous studies.<sup>[12,30,59–61]</sup> Finally, during Stage IV, the

cast is completed, and the mold and extractor along with the attached steel shell are removed from the melt and cooled to room temperature. As a result, the heat fluxes of the mold hot surface decrease.

Figure 15(a) shows a contour map of the reconstructed heat fluxes on the surface of the mold (line AB in Figure 1). The heat flux is approximately  $1.1 \text{ MW m}^{-2}$  around the steel level ( $y$  is 16.5 mm). The maximum mold heat flux recorded was  $2.1 \text{ MW m}^{-2}$  at a location 3.5 to 8.0 mm below the steel level. These values are consistent with many of the reported values in literature.<sup>[1–6,49,62]</sup>

The Power Spectral Density (PSD) of the heat flux was analyzed to examine the fluctuations in heat fluxes near the steel level. The frequency-mold surface position-PSD contour map in Figure 15(b) revealed a range

of heat flux signals with different frequencies and intensities. As previously studies by Badri and Wang *et al.*,<sup>[11,12,59,60]</sup> the mold heat transfer signal consists of both low- and high-frequency components. Low-frequency heat flux is associated with phenomena like the development of shell surface depression, unevenness growth, and level fluctuation, while high-frequency heat flux is linked to the formation of oscillation marks and partial meniscus solidification. A threshold frequency can be used to discern between low- and high-frequency heat fluxes, with fluxes of frequencies higher than the threshold being categorized as high-frequency fluxes. As the width of the shell surface depression is at least twice larger the oscillation mark pitch, the threshold frequency could be set at half the mold oscillation frequency to ensure the low-frequency temperature variations have a period at least twice as long as that of the mold oscillation period. Then, the threshold frequency is set to 0.83 Hz, which is half the mold oscillation frequency ( $f_m$ ) of 1.67 Hz. A strong high-frequency signal of mold heat flux with a frequency of 1.67 Hz was discovered around the liquid steel level (at a depth of 16.5 mm), with a PSD peak value of -8.30 dB/Hz. This suggests that the heat flux around the steel level has a component that oscillates at the same frequency as the mold oscillation. This is likely due to the oscillation-induced heat transfer phenomena caused by the mold oscillation between the slag and the liquid steel.<sup>[10-12]</sup>

The effect of mold oscillation on the mold heat flux decreases along the casting direction. The intensities of high-frequency heat flux signals ( $>0.83$  Hz) decrease, while the intensities of low-frequency heat flux signals ( $<0.83$  Hz) increase as the lower part of the mold is immersed deeper into the molten steel. This phenomenon is attributed to the attenuation of the oscillation-introduced high-frequency effect and the enhancement of the low-frequency effect associated with long-term solidification.<sup>[9,11,12]</sup>

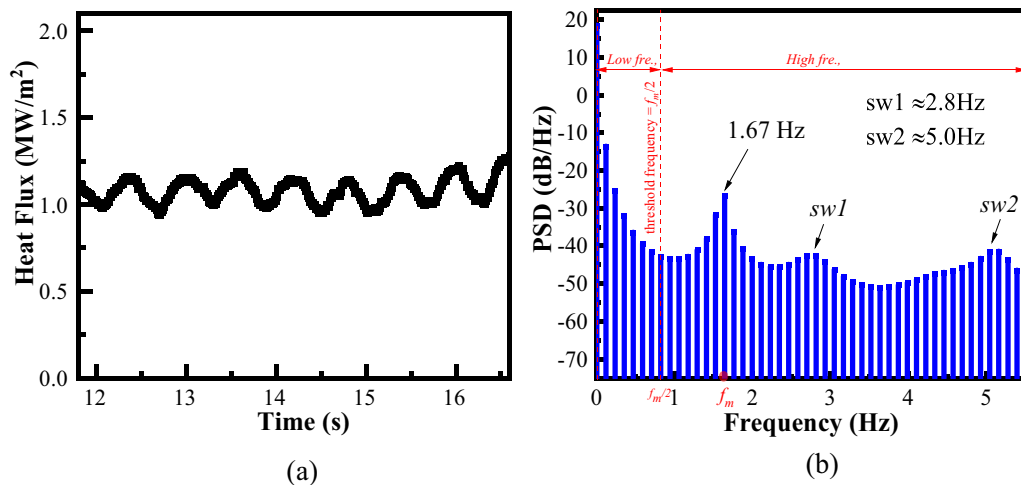


Fig. 16—(a) The mold surface heat fluxes at steel level, and (b) its PSD analysis.

## 2. Change of mold heat flux at the steel level

The mold surface heat flux at the liquid steel level ( $y = 16.5$ mm) during casting is reconstructed through 2DIHCP (Figure 16(a)), and its PSD analyses are illustrated in Figure 16(b). The peak signal shown in Figure 16(b) is around 1.67 Hz in the high-frequency heat flux zone ( $>0.83$  Hz) that is identical to the mold oscillation frequency, which is believed to be introduced by mold oscillation that related to the formation of oscillation mark.<sup>[11,12,59]</sup> Furthermore, there appear two other peaks around 2.8 and 5.0 Hz, which might correspond to the liquid flow at melt-free surface.<sup>[9,30]</sup>

The heat flux at steel level ( $y = 16.5$ mm) is divided into low- and high-frequency components using the FFT low pass filter with a threshold frequency of 0.83 Hz, as shown in Figure 17. It is noticeable that the low-frequency heat flux ( $<0.83$  Hz) displays minor fluctuations around a baseline of 1.1 MW/m², which reflects to long time-scale solidification phenomena

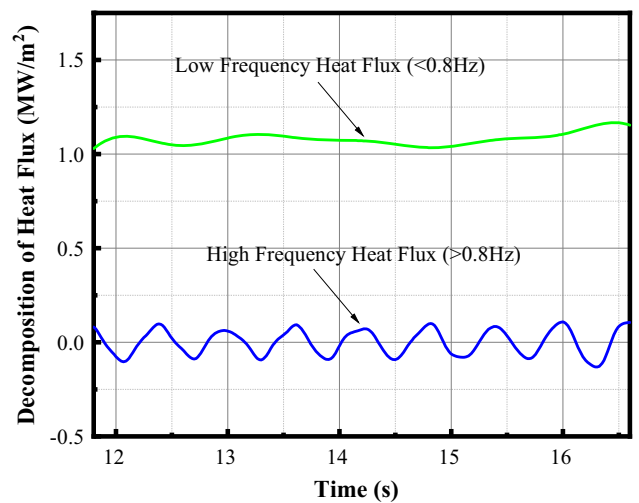


Fig. 17—Decomposition of heat flux at steel level during continuous casting.

during casting, including the formation of shell surface depressions, solidification shrinkage, and irregular solidification of the initial shell.

Figure 18 shows the high-frequency heat fluxes ( $> 0.8$  Hz) during casting. Negative Strip Time (NST) is the period when the mold wall descends faster than the solidified shell, and the remaining period in the cycle is the Positive Strip Time (PST). The heat fluxes for specific positions above/around the steel level (e.g.,  $y = 21$  and  $16.5$  mm) were observed to initially decrease and then increase with the downward motion of the mold. Subsequently, they peak around the early-PST within one cycle of the mold oscillation (NST+PST), and eventually decrease as the mold moves upward. Conversely, the mold surface heat flux for the location below the shell tip (e.g.,  $y = 9$  mm) exhibits an opposite variation pattern compared to those above the liquid steel level. Additionally, the mold surface heat flux for

the position below and away from the liquid steel level presents the smallest variation amplitude ( $0.0158$  MW/m<sup>2</sup>,  $y = 0$  mm), while the heat flux close to the slag level (e.g.,  $y = 16.5$  mm) displays the largest variation amplitude ( $0.1196$  MW/m<sup>2</sup>).

To further analyze the fluctuation of high-frequency heat flux, three typical positions at  $y = 21$  mm (representing the one above the liquid steel level),  $y = 16.5$  mm (representing the liquid steel level), and  $y = 9$  mm (representing the one below the liquid level) during one oscillation cycle are selected from Figure 18, and they are combined and shown with the mold displacement ( $D_m$ ) and velocity ( $V_m$ ) in Figure 19. Our focus is on a single oscillation cycle, spanning from 13.7 to 14.3 seconds, as depicted in Figures 18. The choice of this cycle is because the variations of the heat fluxes during the selected cycle could reflect the variation tendency of most other cycles. At the position above the liquid steel level ( $y = 21$  mm), as the mold descends from the crest T2 to the midway T3, where the mold surface is closing to the liquid steel level, the heat flux experiences an initial decrease to its minimum value, followed by a subsequent increase. This phenomenon can be attributed to the proximity of this part of the mold to the surrounding air at the crest, resulting in cooling effects. As the mold progresses downward and nears the liquid steel, the heat flux experiences a subsequent rise owing to the influence of the liquid steel bath. As mold moves downward from the midway T3 to the trough T4, this part of the mold is entering into the melt, the mold surface heat flux continues to increase as it approaches closer to the liquid steel. When the mold moves upward from the trough T4

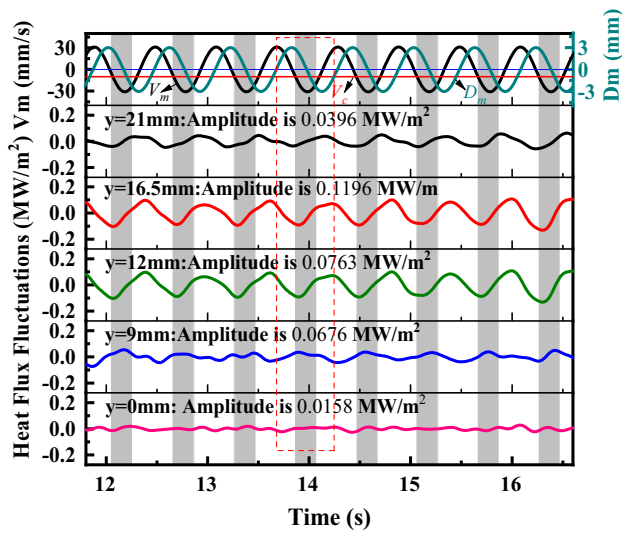


Fig. 18—Variations of high-frequency heat fluxes at different positions of the mold surface during continuous casting.

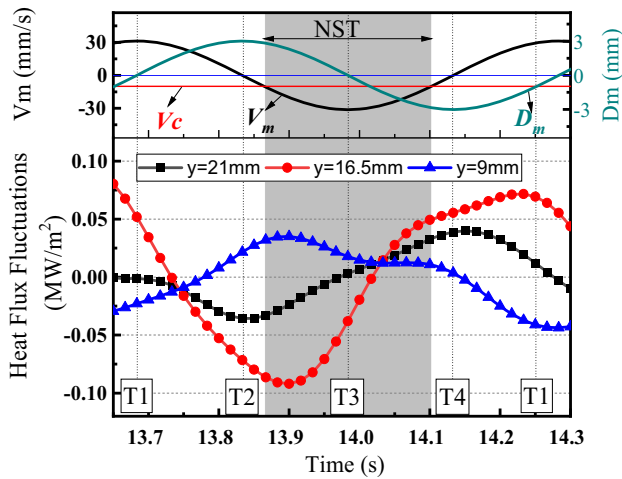


Fig. 19—One cycle of high-frequency heat flux fluctuation. T1 and T3 mark mold Midway position, T2 marks mold crest position, and T4 marks mold trough position.

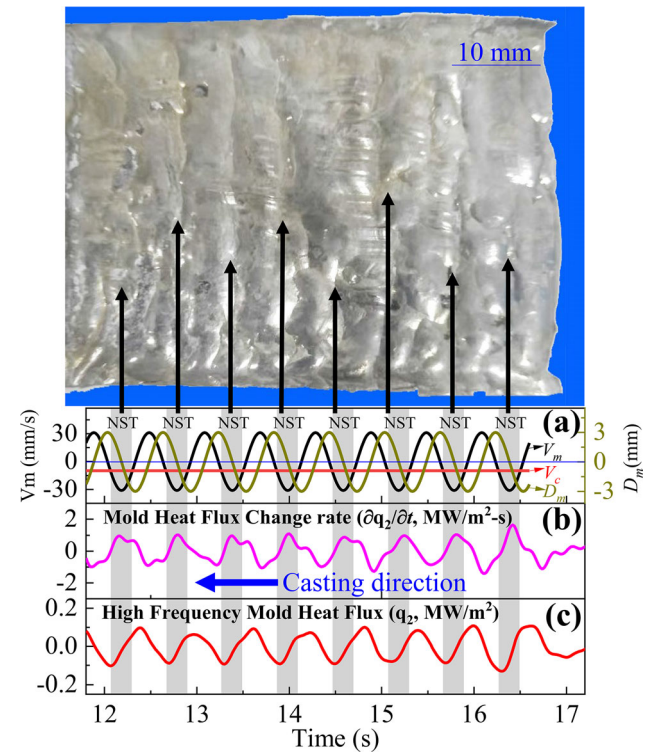


Fig. 20—Relation between the shell surface profile, heat flux, and heat flux variation rate: (a) velocity and displacement of mold, (b) change rate of mold flux, and (c) high-frequency mold heat flux.

to midway T1 where the mold is moving up and moving away from the liquid steel, the mold surface heat flux is observed to increase to the maximum and then decrease in early-PST, as the mold surface location of  $y=21$  mm remains heated by the liquid steel until it moves away from the liquid steel and undergoes cooling from the ambient air. As mold moves ascends from the midway T1 to crest T2, where the mold keeps moving away from the liquid steel, the mold surface heat flux continues to decrease. This decrease can be attributed to this part of the mold being even closer to the surrounding air, resulting in cooling effects from the ambient air. This finding is consistent with the previous studies<sup>[2,4,6,59,60]</sup> as the variation of the heat flux is due to the motion of the mold in/out of liquid slag.

Around the level of the liquid steel ( $y = 16.5$  mm), the mold surface heat flux experiences a rapid increase at mid-NST. This phenomenon arises due to this part of the mold having been immersed in the liquid melt, causing it to be heated by the molten steel when the mold submerges into the bath. The increase of heat flux during this period is also associated with the enhancement of liquid flux infiltration in-between mold/shell gap during NST period<sup>[2,4,6]</sup> and the deformation of the meniscus,<sup>[11,63]</sup> which makes the meniscus further close to the mold.<sup>[10–12]</sup> Therefore, the thermal resistance between the mold and shell gets reduced and the mold is further heated by the meniscus that leads to the increase of the heat flux. Consequently, the growth of the initial shell would be accelerated. During the time between early-PST and the mid-PST (T4 to T1), this part of the mold is moving up from the trough to the midway. During this time, the heat flux attains its peak before subsequently commencing a decline at mid-PST. This is because the mold is continuously heated by the steel melt till it moves out of liquid steel bath and enters the liquid mold flux. During the time between mid-PST and the end-PST (T1 to T2), as the mold ( $y=16.5$  mm) is moving away from the meniscus and enter into the liquid flux layer, the heat flux continues its decline. This decrease persists until it reaches its minimum value, coinciding with the mold is farthest away from the liquid steel bath at the end-PST. This finding is also consistent with the previous experimental studies,<sup>[10–12,60]</sup> due to the partial meniscus solidification during the NST, and the simulation observation.<sup>[2,4,6,62]</sup>

Below the liquid steel level ( $y = 9$  mm), as the mold descends from the crest T2 down to the trough T4, this part of the mold further immerses into the liquid steel. The mold surface heat flux first initially experiences a slight increase to reach its maximum value, followed by a subsequent decrease. This pattern is contrary to the trends observed at the other two positions. This phenomenon occurs due to the mold's downward motion (originating from the meniscus area) toward a position located deeper within the liquid bath. Throughout this process, the thermal resistance between the mold and the shell tends to increase with the growth of the shell thickness and further crystallization of mold flux layer.<sup>[12,59,64,65]</sup> As the mold ascends from the trough T4 to the crest T2, the heat flux first decreases to the minimum at mid-PST after which it subsequently rises. This phenomenon emerges because the mold is ascending toward the steel level, leading to a reduction in the corresponding thermal resistance. This finding is consistent with the previous simulation results.<sup>[2,4,6,12,62]</sup>

Figure 20 illustrates the correlation among the displacement and velocity of the mold oscillation, the high-frequency heat flux ( $q_2$ ) at the steel level ( $y = 16.5$  mm), and its rate of heat flux variation ( $\partial q_2/\partial t$ ). The oscillation marks produced within the oscillation cycle manifest as periodic transverse depressions on the surface of the shell. Theoretical considerations indicate that each mold oscillation corresponds to the generation of a single oscillation mark. Consequently, the spacing or pitch of these oscillation marks is denoted as  $V_c/f_m$ . The measured pitch of these oscillation marks is  $5.98 \pm 0.13$  mm, exhibiting a close alignment with the theoretical value of 6 mm. It is clearly shown that the heat flux increases rapidly when mold downstroke during NST period. Additionally, the maximum value of the heat flux variation rate occurs during NST period. Notably, the occurrence of each oscillation mark on the shell surface corresponds to a peak in the variation rate. This observation implies that the sudden rise in heat flux is directly linked to the formation of oscillation marks. This robustly suggests that the formation of oscillation marks is tied to a release of energy at the steel level that can be measured thermocouple measurements within the mold. The oscillation mark is formed by one of the two different formation mechanisms.<sup>[6,11]</sup> One mechanism involves the solidified shell with a partially solidified meniscus being bent backward toward the mold wall due to the ferrostatic pressure of the liquid steel. This results in the formation of a depression-type oscillation mark. The second mechanism involves the liquid steel overflowing to the shell tip, creating a hook-type mark. This occurs if the initial shell is strong enough to withstand the ferrostatic pressure. Furthermore, it is noteworthy that the heat flux peak is observed either during end-NST or early-PST. This observation implies that at these times during the experiment, the partial solidified meniscus is bent back toward the mold or the liquid steel overflows to the shell tip, leading to the formation of an oscillation mark.<sup>[6]</sup>

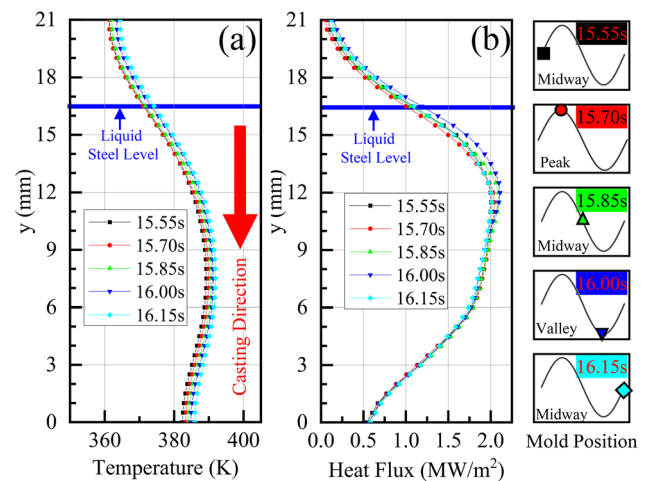


Fig. 21—Recovered thermal field at mold surface during continuous casting: (a) Heat flux and (b) Temperature.

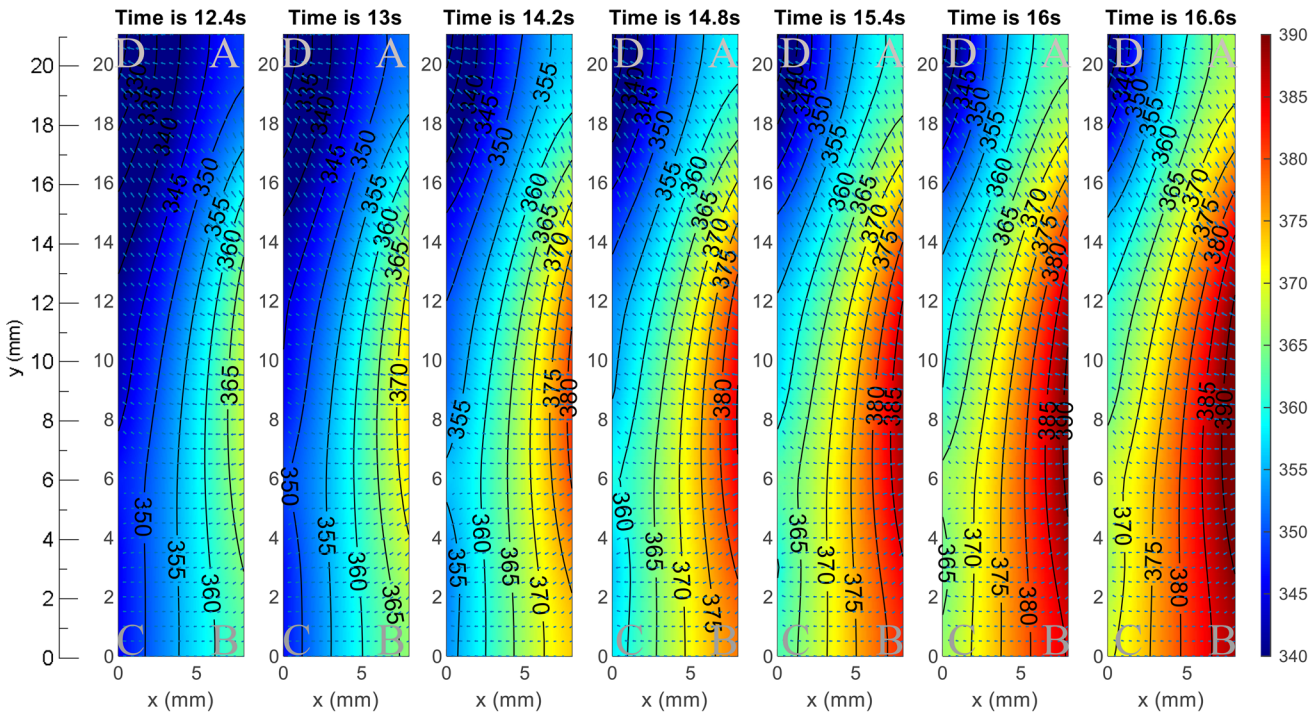


Fig. 22—Thermal evolution of the mold wall during the casting.

### 3. Charge of mold heat flux along the casting direction

Figure 21 shows how mold heat flux fluctuates along the casting direction during a mold oscillation cycle at different times, namely 15.55, 15.70, 15.85, 16.00, and 16.15 seconds, as represented by the blue lines in Figure 15(a). These times correspond to the midway, peak, midway, valley, and midway of the mold oscillation, respectively. The maximum mold heat flux of  $2.1 \text{ MW m}^{-2}$  is located 4.5 mm below the steel level along the casting direction. On the other hand, the maximum mold temperature of 394 K can be found 9.3 mm below the steel level. It is observed that the mold heat flux fluctuates more significantly near the steel level, which is consistent with the variation pattern of high-frequency heat flux shown in Figure 15(b).

Figure 22 shows the temperature evolution of the mold wall (the rectangle area ABCD in Figure 1) during the casting process (stage III in Figure 12). As the initial shell is withdrawn downward, the temperature of the mold hot surface below the liquid steel ( $y < 16.5 \text{ mm}$ ) increases and reaches a maximum of 394 K at the end of the casting process, which corresponds to a depth of 9.3 mm below the steel level. The heat flux direction within the mold wall is also illustrated in Figure 22, where the arrows indicate the direction of the heat flow. The predominant mode of heat transfer is along the  $x$ -axis for the mold wall below the location of the maximum mold surface temperature (394 K,  $y$  is 9.3 mm). A significant amount of heat is transferred upward for the mold wall above the location of the maximum mold surface temperature, while a small fraction of the heat flowing downward to the location below the maximum mold surface temperature. This is due to the

upper part of the mold being exposed to air, resulting in a lower temperature and a temperature gradient inside the mold, leading to vertical heat transfer along the  $y$ -axis.<sup>[12,30]</sup>

In conclusion, a methodology that combines the L-curve technique with Morosov's criterion is utilized to determine the appropriate number of future steps ( $r$ ) and the regularization parameter ( $\alpha$ ). The oscillation of the mold has a discernible impact on the mold heat flux. This effect is more pronounced in the proximity of the steel level and diminishes gradually along the direction of the casting.

## V. CONCLUSIONS

This study examines the effects of the depth of thermocouples beneath mold surface ( $w_1$ ), the temperature sampling rate ( $f_s$ ), and the noise level of temperature data ( $\sigma$ ), on the accuracy of 2DIHCP for heat flux estimations. To optimize the selection of the number of future steps ( $r$ ) and the regularization parameter ( $\alpha$ ), a method combining the L-curve method and Morosov's criterion is proposed. The 2DIHCP is then utilized to estimate the heat flux in a mold simulator experiment. The main conclusions are made as follows:

1. The accuracy of heat flux estimations utilizing temperatures from thermocouples positioned 1 to 3 mm away from the mold surface exceeds that of estimations relying on temperatures from thermocouples situated 5 mm away from the mold surface. It is advisable to ensure the distance does not exceed 3 mm.

2. The accuracy of heat flux estimations initially increases with the temperature sampling rate ( $f_s$ ) from 5 to 10 Hz, then remains relatively stable when  $f_s$  increases from 10 to 60 Hz, and finally decreases when  $f_s$  increases from 60 to 100 Hz. Both first- and second-order spatial regularizations are more accurate than zeroth-order spatial regularization when a high-temperature sampling rate is used.
3. The accuracy in heat flux estimations decreases with increasing temperature measurement error. First-order spatial regularization is more precise than both zeroth- and second-order spatial regularizations when the temperature measurement contains errors.
4. The 2DIHCP is successfully applied to reconstruct the heat flux across an oscillating mold surface for a mold simulator experiment. The mold heat flux at the meniscus level during the time lapse of a mold oscillation cycle is reconstructed.

## ACKNOWLEDGMENTS

The authors wish to acknowledge Mr. Xiong Yan at the School of Metallurgy and Environment, Central South University, China, for his help in interpreting the significance of the variation of heat flux in this study. The financial supports from NSFC (No. 52074135), Jiangxi Provincial Natural Science Foundation (No. 20224ACB214011), and Youth Jinggang Scholars Program in Jiangxi Province (QNJG2020049) are greatly acknowledged.

## CONFLICT OF INTEREST

The authors declare that they have no conflict of interest.

## APPENDIX A: SENSITIVITY COEFFICIENT MATRIX

$\mathbf{J}_j$  is called as the  $M \times N$  sensitivity coefficient matrix at time  $t_j$  and is defined as follows:

$$\mathbf{J}_j = \left[ \frac{\partial \mathbf{T}(\mathbf{q}^j)}{\partial \mathbf{q}^j} \right]^T = \begin{pmatrix} J_{1,1}^j & J_{1,2}^j & \cdots & J_{1,N}^j \\ J_{2,1}^j & J_{2,2}^j & \cdots & J_{2,N}^j \\ \vdots & \vdots & \ddots & \vdots \\ J_{M,1}^j & J_{M,2}^j & \cdots & J_{M,N}^j \end{pmatrix}, \text{ where } J_{m,n}^j = \frac{\partial T_m^j}{\partial q_n^j} \quad [\text{A1}]$$

$J_{m,n}^j$  represents the temperature rise at the sensor location  $(x_m, y_m)$  in response to a unit step change in the heat flux at point  $(x_n, y_n)$  on boundaries  $\Gamma_1$ ,  $\Gamma_2$ , and  $\Gamma_3$ , at time  $t_j$ . To obtain the sensitivity coefficient problem, the partial derivative of Eqs. [2b] through [2e] is taken

with respect to a heat flux component  $q_n^j$ , (Eq. [A1]), which yields the governing sensitivity coefficient problem.

$$\frac{\partial J}{\partial t} = \frac{\partial^2 J}{\partial x^2} + \frac{\partial^2 J}{\partial y^2}, 0 < t \leq t_r \text{ in } \Omega = [0, W] \times [0, H]. \quad [\text{A2a}]$$

$$-\frac{\partial J}{\partial \mathbf{n}} \Big|_{\Gamma_1 \cup \Gamma_2 \cup \Gamma_3} = \begin{cases} 1, & (x, y) = (x_n, y_n) \\ 0, & \text{others} \end{cases} \quad [\text{A2b}]$$

$$J|_{\Gamma_4} = 0 \quad [\text{A2c}]$$

$$J(x, y, 0) = 0 \quad [\text{A2d}]$$

## REFERENCES

1. R.B. Mahapatra, J.K. Brimacombe, and I.V. Samarasekera: *Metall. Mater. Trans. B*, 1991, vol. 22B, pp. 875–88.
2. X. Zhang, W. Chen, Y. Ren, and L. Zhang: *Metall. Mater. Trans. B*, 2019, vol. 50B, pp. 1444–60.
3. H. Mizukami, Y. Shirai, and S. Hiraki: *ISIJ Int.*, 2020, vol. 60(9), pp. 1968–77.
4. J. Yang, Z. Cai, D. Chen, and M. Zhu: *Metall. Mater. Trans. B*, 2019, vol. 50B, pp. 1104–13.
5. J. Ji, Y. Cui, X. Zhang, Q. Wang, S. He, and Q. Wang: *Steel Research International*, 2021, vol. 92(10), p. 2100101.
6. P.E.R. Lopez, K.C. Mills, P.D. Lee, and B. Santillana: *Metall. Mater. Trans. B*, 2012, vol. 43B(1), pp. 109–22.
7. J.K. Brimacombe: *Can. Metall. Q.*, 1976, vol. 15(2), pp. 163–75.
8. J.A. Kromhout, E.R. Dekker, M. Kawamoto, and R. Boom: *Ironmak. Steelmak.*, 2013, vol. 40(3), pp. 206–15.
9. R.J. O'Malley: *Steelmak. Conf. Proc.*, 1999, vol. 82, pp. 13–34.
10. H. Zhang, W. Wang, F. Ma, and L. Zhou: *Metall. Mater. Trans. B*, 2015, vol. 46B(5), pp. 2361–73.
11. A. Badri, T.T. Natarajan, C.C. Snyder, K.D. Powers, F.J. Mannion, M. Byrne, and A.W. Cramb: *Metall. Mater. Trans. B*, 2005, vol. 36B(3), pp. 373–83.
12. H. Zhang and W. Wang: *Metall. Mater. Trans. B*, 2016, vol. 47B(2), pp. 920–31.
13. C.E. Shannon: *Proc. IRE*, 1949, vol. 37(1), pp. 10–21.
14. M. Roman, D. Balogun, C. Zhu, L. Bartlett, R.J. O'Malley, R.E. Gerald, and J. Huang: *IEEE Trans. Instrum. Meas.*, 2021, vol. 70, pp. 1–10.
15. J.V. Beck, B. Blackwell, and C.R. Clair Jr: *Inverse Heat Conduction: Ill-Posed Problems*, James Beck, 1985, pp. 1–300.
16. G. Blanc, M. Raynaud, and T.H. Chau: *Revue générale de thermique*, 1998, vol. 37(1), pp. 17–30.
17. Y. Liu, Z. Xu, X. Wang, and D. Zhang: *Ironmak. Steelmak.*, 2021, vol. 48(8), pp. 901–08.
18. M.O. Ansari, J. Ghose, S. Chattopadhyaya, D. Ghosh, S. Sharma, P. Sharma, A. Kumar, C. Li, R. Singh, and S.M. Eldin: *Micro-machines*, 2022, vol. 13(12), p. 2148.
19. A.V.S. Oliveira, A. Avrit, and M. Gradeck: *Int. J. Heat Mass Transf.*, 2022, vol. 185, 122398.
20. D. Balogun, M. Roman, R.E. Gerald, L. Bartlett, J. Huang, and R. O'Malley: *Metall. Mater. Trans. B*, 2023, vol. 54B(3), pp. 1326–41.
21. M.N. Özisik and H.R. Orlande: *Inverse Heat Transfer: Fundamentals and Applications*, CRC Press, Boca Raton, 2021, pp. 3–111.
22. A.S. Vaka, S. Ganguly, and P. Talukdar: *Int. J. Therm. Sci.*, 2021, vol. 160, 106648.

23. C.A.M. Pinheiro, I.V. Samarasekera, J.K. Brimacombe, and B.N. Walker: *Ironmak. Steelmak.*, 2000, vol. 27(1), pp. 37–54.
24. B.G. Thomas, M.A. Wells, and D. Li: *Sensors, Sampling, and Simulation for Process Control*, 2011, pp. 119–26.
25. X. Wang, L. Tang, X. Zang, and M. Yao: *J. Mater. Process. Technol.*, 2012, vol. 212, pp. 1811–18.
26. P. Hu, X. Wang, J. Wei, M. Yao, and Q. Guo: *ISIJ Int.*, 2018, vol. 58, pp. 892–98.
27. E.N. Dvorkin, M.A. Cavaliere, and M.B. Goldschmit: *Comput. Struct.*, 2003, vol. 81, pp. 559–73.
28. M. Gonzalez, M.B. Goldschmit, A.P. Assanelli, E.N. Dvorkin, and E.F. Berdaguer: *Metall. Mater. Trans. B*, 2003, vol. 34B, pp. 455–73.
29. S. Chakraborty, S. Ganguly, E.Z. Chacko, S.K. Ajmani, and P. Talukdar: *Int. J. Therm. Sci.*, 2017, vol. 118, pp. 435–47.
30. H. Zhang, W. Wang, and L. Zhou: *Metall. Mater. Trans. B*, 2015, vol. 46B(5), pp. 2137–52.
31. P. Jayakrishna, S. Chakraborty, S. Ganguly, and P. Talukdar: *Can. Metall. Q.*, 2021, vol. 60(4), pp. 320–49.
32. T. Rees, H.S. Dollar, and A.J. Wathen: *SIAM J. Sci. Comput.*, 2010, vol. 32(1), pp. 271–98.
33. Y. Yu and X. Luo: *Int. J. Heat Mass Transf.*, 2015, vol. 90, pp. 645–53.
34. I. Nowak, J. Smolka, and A.J. Nowak: *Appl. Therm. Eng.*, 2010, vol. 30(10), pp. 1140–51.
35. M. Cui, Y. Zhao, B. Xu, and X.W. Gao: *Int. J. Heat Mass Transf.*, 2017, vol. 107, pp. 747–54.
36. B. Zhang, J. Mei, M. Cui, X.W. Gao, and Y. Zhang: *Int. J. Heat Mass Transf.*, 2019, vol. 140, pp. 909–17.
37. Y. Yu and X. Luo: *Appl. Therm. Eng.*, 2017, vol. 114, pp. 36–43.
38. Y. Li, G. Wang, and H. Chen: *Appl. Therm. Eng.*, 2015, vol. 80, pp. 396–403.
39. B.A. Tourn, J.C. Hostos, and V.D. Fachinotti: *Int. Commun. Heat Mass Transf.*, 2023, vol. 142, 106647.
40. Y. Zeng, H. Wang, S. Zhang, Y. Cai, and E. Li: *Int. J. Heat Mass Transf.*, 2019, vol. 134, pp. 185–97.
41. G. Wang, S. Wan, H. Chen, K. Wang, and C. Lv: *J. Heat Transf.* 2018, vol. 140(12), pp. 122301.
42. Y. Li, H. Wang, and X. Deng: *Int. J. Heat Mass Transf.*, 2019, vol. 134, pp. 656–67.
43. F. Zhu, J. Chen, Y. Han, and D. Ren: *Int. J. Heat Mass Transf.*, 2022, vol. 194, 123089.
44. B.A. Tourn, J.C. Hostos, and V.D. Fachinotti: *Int. Commun. Heat Mass Transf.*, 2021, vol. 127, 105488.
45. J.V. Beck: *Int. J. Heat Mass Transf.*, 1970, vol. 13, pp. 703–16.
46. C.U. Ahn, C. Park, D.I. Park, and J.G. Kim: *Int. J. Heat Mass Transf.*, 2022, vol. 183, 122076.
47. K. Babu and T.S.P. Kumar: *Metall. Mater. Trans. B*, 2010, vol. 41B, pp. 214–24.
48. B.A. Tourn, J.C. Hostos, and V.D. Fachinotti: *Int. Commun. Heat Mass Transf.*, 2021, vol. 125, 105330.
49. A. Badri, T.T. Natarajan, C.C. Snyder, K.D. Powers, F.J. Mannion, and A.W. Cramb: *Metall. Mater. Trans. B*, 2005, vol. 36B(3), pp. 355–71.
50. X. Xie, D. Chen, H. Long, M. Long, and K. Lv: *Metall. Mater. Trans. B*, 2014, vol. 45B(6), pp. 2442–52.
51. P.C. Hansen: *Numerical Algorithms*, 1994, vol. 6(1), pp. 1–35.
52. H.R. Orlande, O. Fudym, D. Maillet, and R.M. Cotta: *Thermal Measurements and Inverse Techniques*, CRC Press, Boca Raton, 2011, pp. 233–619.
53. L. Olson and R. Throne: *Inverse Prob. Eng.*, 2000, vol. 8(3), pp. 193–227.
54. R.C. Aster, B. Borchers, and C.H. Thurber: *Parameter Estimation and Inverse Problems*, Elsevier, New York, 2018, pp. 93–252.
55. K.A. Woodbury and J.V. Beck: *Int. J. Heat Mass Transf.*, 2013, vol. 62, pp. 31–39.
56. C.R. Vogel: *Computational Methods for Inverse Problems*, Society for Industrial and Applied Mathematics, Philadelphia, 2002, pp. 97–124.
57. M.N. Özisik: *Heat Conduction*, 2nd ed. Wiley, New York, 1993, pp. 62–75.
58. S. Khajehpour, M.R. Hematiyan, and L. Marin: *Int. J. Heat Mass Transf.*, 2013, vol. 58(1–2), pp. 125–34.
59. H. Zhang and W. Wang: *Metall. Mater. Trans. B*, 2017, vol. 48B(2), pp. 779–93.
60. W. Wang, X. Long, H. Zhang, and P. Lyu: *ISIJ Int.*, 2018, vol. 58(9), pp. 1695–704.
61. A. Kamaraj, S. Tripathy, G. Chalavadi, P.P. Sahoo, and S. Misra: *Steel Res. Int.*, 2022, vol. 93(3), p. 2100121.
62. A.S. Jonayat and B.G. Thomas: *Metall. Mater. Trans. B*, 2014, vol. 45B, pp. 1842–64.
63. A. Matsushita, K. Isogami, M. Takeyoshi, T. Ninomi, and K. Tsutsumi: *Trans. Iron Steel Inst. Jpn.*, 1988, vol. 28, pp. 531–34.
64. E.Y. Ko, J. Choi, J.Y. Park, and I. Sohn: *Met. Mater. Int.*, 2014, vol. 20, pp. 141–51.
65. J.Y. Park, E.Y. Ko, J. Choi, and I. Sohn: *Met. Mater. Int.*, 2014, vol. 20, pp. 1103–14.

**Publisher's Note** Springer Nature remains neutral with regard to jurisdictional claims in published maps and institutional affiliations.

Springer Nature or its licensor (e.g. a society or other partner) holds exclusive rights to this article under a publishing agreement with the author(s) or other rightsholder(s); author self-archiving of the accepted manuscript version of this article is solely governed by the terms of such publishing agreement and applicable law.